scientific reports

OPEN

Partial differential equations of entropy analysis on ternary hybridity nanofluid flow model via rotating disk with hall current and electromagnetic radiative influences

Khalid Fanoukh Al Oweidi[1], Faisal Shahzad[2], Wasim Jamshed[2✉], Usman[3], Rabha W. Ibrahim[4], El Sayed M. Tag El Din[5] and Sayed M. AlDerea[6]

The flow of a fluid across a revolving disc has several technical and industrial uses. Examples of rotating disc flows include centrifugal pumps, viscometers, rotors, fans, turbines, and spinning discs. An important technology with implications for numerous treatments utilized in numerous sectors is the use of hybrid nanofluids (HNFs) to accelerate current advancements. Through investigation of ternary nanoparticle impacts on heat transfer (HT) and liquid movement, the thermal properties of tri-HNFs were to be ascertained in this study. Hall current, thermal radiation, and heat dissipation have all been studied in relation to the use of flow-describing equations. The ternary HNFs under research are composed of the nano molecules aluminum oxide (Al_2O_3), copper oxide (CuO), silver (Ag), and water (H_2O). For a number of significant physical characteristics, the physical situation is represented utilizing the boundary layer investigation, which produces partial differential equations (PDEs). The rheology of the movement is extended and computed in a revolving setting under the assumption that the movement is caused by a rotatingfloppy. Before the solution was found using the finite difference method, complicated generated PDEs were transformed into corresponding ODEs (Keller Box method). A rise in the implicated influencing factors has numerous notable physical impacts that have been seen and recorded. The Keller Box method (KBM) approach is also delivered for simulating the determination of nonlinear system problems faced in developing liquid and supplementary algebraic dynamics domains. The rate of entropy formation rises as the magnetic field parameter and radiation parameter increase. Entropy production rate decreases as the Brinkman number and Hall current parameter become more enriched. The thermal efficiency of ternary HNFs compared to conventional HNFs losses to a low of 4.8% and peaks to 5.2%.

List of symbols

c	Initial stretching rate
u, v, w	Speed components (ms^{-1})
r, φ, z	Cylinder-shaped coordinates

[1]Department of Water Resources Management Engineering, College of Engineering, Al-Qasim Green University, Babylon, Iraq. [2]Department of Mathematics, Capital University of Science and Technology (CUST), Islamabad 44000, Pakistan. [3]Department of Computer Science, National University of Sciences and Technology, Balochistan Campus (NBC), Quetta 87300, Pakistan. [4]Department of Mathematics, Mathematics Research Center, Near East University, Near East Boulevard, 99138 Nicosia/Mersin 10, Turkey. [5]Departement of Electrical Engineering, Faculty of Engineering and Technology, Future University, New Cairo 11835, Egypt. [6]Department of Mathematics, College of Science and Arts, Qassim University, Al-Badaya, 51951, Saudi Arabia. ✉email: wasiktk@hotmail.com

C_p	Particular thermal ($\mathrm{Jkg^{-1}K^{-1}}$)
S	Unsteadiness parameter (s)
ω	Rotation parameter
b	Positive constant
κ	Thermal conductivity ($\mathrm{Wm^{-1}K^{-1}}$)
k^*	Concentration constant
Nr	Radiation parameter
m	Hall movement bound
Nu_r	Local Nusselt constant
Pr	Prandtl number (ν/α)
q_r	Radiative heat flux ($\mathrm{kgs^{-3}}$)
Re	Reynolds number
ϕ_1, ϕ_2, ϕ_3	Volume fractions
ω_e	Cyclotron frequency of electron (Hz)
τ_e	Electron collision
Pe	Pressure of electron (Pa)
n_e	Number of density
μ_e	Magnetic permeability of electron ($\mathrm{Hm^{-1}}$)

Greek symbols

¥	Fluid heat (K)
$¥_0$	Source heat (K)
$¥_{ref}$	Orientation heat (K)
ϕ	Solid volume fraction
ρ	Density ($\mathrm{Kgm^{-3}}$)
σ^*	Stefan Boltzmann constant
Ec	Eckert number
Ω	Angular speed ($\mathrm{rad\,s^{-1}}$)
μ	Self-motivated viscidness of the liquid ($\mathrm{kgm^{-1}s^{-1}}$)
ν	Kinematic thickness of the liquid ($\mathrm{m^2s^{-1}}$)
$F^{*'}$	Radial velocity
ξ	Independent similarity variable
θ^*	Temperature (dimensionless)
G^*	Azimuthal velocity

Subscripts

f	Improper fluid
nf	Nanofluid
m, t, h	Mono, tri, hybrid
CuO	Copper oxide nanoparticles
Al_2O_3	Aluminium oxide nanoparticles
Ag	Silver nanoparticles

The generation, utilization, conversion, and exchange of heat through physical configurations are the topics of heat transfer (thermal transform) (TT), an area of contemporary engineering. Heat is transferred through a variety of techniques, including heat transmission, convection current, current radiation, and energy loss via phase variations. Engineers likewise consider the all types of transfers (heat, mass amd heat-mass) of different chemical classes in order to realize TT (mentioned to as physical announcement in the technique of the movement of a fluid, especially horizontally in the air or water, to transmit heat or substance). These developments are different, although they regularly happen instantaneously in the identical scheme. A variety of TT problematic examples are currently being measured by investigators. The neural networks are selected by Cai et al.[1] for TT experiments. Mousa et al.[2] presented a review investigation in which they improved methods by eating TT. In the research of Li et al.[3], transformed properties are promoted in combination with TT. The effort of Khodadadi et al.[4] requires the effectiveness of TT and electrical performance calculation of possessions. Sheikholeslami et al.[5] developed a scientific demonstrating outline aimed at regulating TT. Nguyen et al.[6] obtained a detailed assessment of TT. Mohankumar, et al.[7] proposed TT through countless classes of geometries. Additional TT presentations can be found in solar researches[9], magnetic fields[8], and altering macroscopic[10]. Gao et al.[11], Jiaqiang et al.[12], and Mousavi et al.[13] have recently reviewed the application of TT in the field of energy.

There are several simulations available to outbuilding light on the performance of hybrid nanofluids (HNFs), containing the controller regulation structure, Carreaus arrangement, Cross system, and Ellis pattern; however, the Williamson liquid strategy has received little attention from academics (WLS). Williamson (1929) supposed the flow of HNFs as a system of equations and then confirmed the results. Researchers suggested in a sophisticated gravitational analysis that a WLS's reverberating level should move to the conclusion of an inspired superficial. With respect to its molecular structure, a real fluid possesses together the deepest and maximum operational viscosities. The lowest and maximum thicknesses are measured together by the WLS. Said et al.[14] invisaged a 3D-class of HNF in the event of a revolution in order to additional progress the amount of heat transfer (HT)

by broadening slide. Investigative statistics were created using an artificial neural network by Mandal et al.[15]. Al-Chlaihawi et al.[16], Saha et al.[17] reported a research of HNFs' rheological and TT properties for refrigeration presentations. Researcheres in[18–20] have all published survey studies in this area. While a small investigation on mechanical revisions was performed in HNF by Dubey et al.[21]. The migration of an MHD tangent HNF across a stretched slip's boundary layer was examined by Syed and Jamshed[22]. Additionally, the demonstration of the prolonged TT of curvature hyperbolic liquids across a nonlinearly oscillating transparency incorporating HNFs was put to the test by Qureshi[23], Jamshed et al.[24], and Parvin et al.[25].

Three separate single nanofluid types were used to prepare tri-hybrid nanofluids (THNFs). Sahu et al.[26] investigated the stable-formal and passing hydrothermal studies of solitary-stage normal measure ring employing aquatic-based THNFs. Safieiet al.[27] computed the possessions of THNFs going on shallow roughness and upsetting heat in close overwhelming procedure of aluminum mixture utilizing uncoated and covered sharp inserts with negligible amount lubricant technique. Manjunatha et al.[28] presented a hypothetical realization of convective TT in THNFs fluid past a extending slip. Gul and Saeed[29] introduced a varied convection pair pressure THNFs movement in a Darcy-Forchheimerabsorbentaverage via a nonlinear extending shallow. Ramadhan et al.[30–32] considered an investigational examination of thermo-physical possessions of THNFs in water-ethylene glycol assortment.

The result of converting the THNFs flow, wind, and current to the construction associated an unsteady flow analysis (UFA), which develops in line with cyclone molting. In their numerical study of spit-up and inactivity sites for stable and UFA via an elliptic cylinder next to aaffecting wall, Zhu and Holmedal[33] developed their methodology. In simplified and accurate iliac bifurcation replicas, Carvalho et al.[34] considered a numerical investigation of the UFA. The UFA field in the humanoid pulmonic was once again numerically reproduced by Ciloglu[35]. In a rotating annulus area with a control law kernel, Javaid et al.[36] reported UFA of fractional Burgers' fluid. UFA in a side station pump with a curved blade was described by Zhang et al.[37]. Phan and He[38] investigated UFA's efficiency when demonstrating for bladerows that were randomly misaligned and subjected to inlet modification. In arrow-shaped micro-mixers with various slope approaches, Mariotti et al.[39] presupposed UFA. Through distribution and deep-learning-based denoising, Wu et al.[40] prepared a deep study on UFA. UFA of a wavering piezoelectric fan blade at high Reynolds numbers was employed by Chen et al.[41]. Li et al.[42] proposed a dynamic delayed detached-eddy model and an investigation on UFA's acoustic equivalency.

Rotating discs are a common component of many mechanical structures, containing flywheels, mechanisms, footbrakes, and gas turbine appliances. The level of force required to push the loop past frictional effort is determined by the shave pressures between the disk and the rotating liquid, and the local movement field will move TT. Numerous factors conspire haphazardly to prevent any common analysis, therefore it is important to take movement aspects and the contiguity of limited geometry into consideration. Suliman et al.[43] used the inside helical flippers on revolving discs enhanced the competence and PEC of a parabolic solar collector including THNFs. The dynamism propensity founded by means of THNFs and altered via a strong magnetic field across rotating discs was analyzed using finite elements by Hafeez et al.[44]. A mathematical preparation on TT and mass transmission in Maxwell liquid with THNFs was presented by Haneef et al.[45] utilizing spinning discs. THNFs with TT over vertical heated cylinder were the subject of an investigation by Nazir et al.[46,47]. Darcy THNFs movement over a scattering pipe with thinning possessions remained computationally valued in the effort of Alharbi et al.[48].

Thermal radiation (TR) is electromagnetic energy that is created through a material as a consequence of its temperature and whose physiognomies depend on the material's temperature. An example of TR is the infrared radiation given off by a conventional internal radiator or electric heater. A review paper on HS, TR, and heat transmission of thin porous media was offered by Xu et al.[49]. Alumina-copper oxide hybrid NFs' thermo-magnetohydrodynamic constancy was examined by Wakifet al.[50] by looking at the TR properties. Studying the impact of NPs aggregation on NFs' TR holdings was done by Chen et al.[51]. The flow of Al_2O_3 NFs with TR and HS effects was controlled by Agrawal et al.[52] over an expanse of seemingly entrenched porous material. Magnetic NFs with TR and properties of heat-dependent viscosity were pumped using peristaltic motion by Prakash et al.[53]. Zhang et al.[54] created a magnetic dipole and TR influences on stagnation point movement of micropolar based NFs across a precipitously extending slip using the finite element approach. In light of TR and motive energy, Ali et al.[55] offered a comparative study of trembling MHD Falkner-Skan wedge flow for non-Newtonian NFs. For any Prandtl number, Shaw et al.[56] used the MHD movement of Cross HNFs influenced by linear, nonlinear, and quadratic TR.

The current, which is recognized as a Hall current, is present constantly but an electric field is applied to an electrode that likewise has an MHD (HC: after the Hall Upshot). Ramzan et al.[57] investigated the migration of THNFs derived from mildly ionized kerosene oil over a convectively animated rotating surface. In ethylene glycol, Wang et al.[58] provided a method for combining THNFs that included moveable diffusion and current conductivity utilizing a non-scheme. Fourier's A study of THNFs distributionclasses and energy transmission in materials affected by input energy and heat source was recommended by Sohail et al.[59,60]. A large manufacturing of current energy in partially ionized hyperbolic tangent material formulated by ternary THNFs was disclosed by Nazir et al.[61].

Recently, many researchers utilized THNFs with viscous dissipation (VD). Khan et al.[62] studied the movement and TT of bio–convective THNFs stratification effects. Zainal et al.[63] described the VD and MHD THNFs flow towards an exponentially stretching/shrinking surface. Hou et al.[64] presented the dynamics of THNFs in the rheology of pseudo-plastic liquid with some material effects. Khan and Haleema[65] studied the thermal performance in THNFs under the influence of mixed convection and VD by using a numerical investigation. Munawar and Saleem[66] varied convective cilia activatedwatercourse of magneto ternary THNFs by elastic pump and VD using the entropy analysis.

It is well knowledge that the entropy, a consequence of any thermal activity, measures the degree of irreversibility. Cooling and warming are key cases that are usually employed in energy and electrical equipment in a
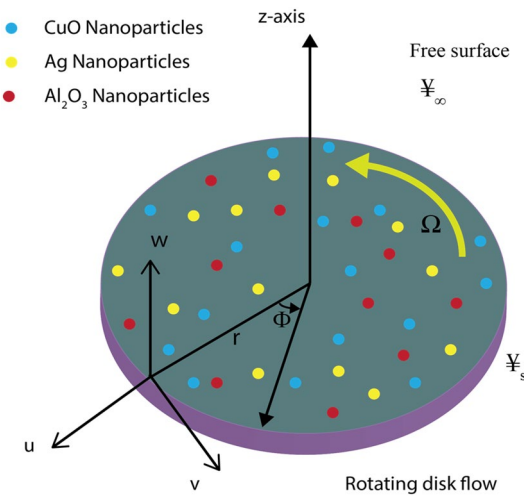
Figure 1. Diagramillustration of the movementmodel.

number of industrial engineering research disciplines[67]. Shahsavar et al.[68] conducted a statistical analysis of the entropy generation of the HNF flow. Significant improvements in NFs properties relative to straight fluids have contributed to the quick development of using HNFs for TT proposed by Hussien et al.[69]. The effects of MHD and TT movement with maximal entropy is presented by Ellahi et al.[70]. While, Lu et al.[71] investigated the non-linear heating system by using the entropy concept in movement of HNF done by a slip. The maximization of entropy is used in recent research by Sheikholeslami et al.[72], Khan et al.[73], Zeeshan et al.[74], Ahmad et al.[75], and Moghadasi et al.[76]. Entropy was recommended by Jamshed et al.[24,77,78] to optimize thermal applications, while Shahzad et al.[79] used it to growth the currenteffectiveness of a solar water pump used in NFs movement. References[80–86] did similar work.

The TT of tri-HNFs over a rotating disk by means of linear dynamism, Hall movement, and heat depravities, or else the collaborating of ternary HNFs in MHD movement, have not been studied before. The ternary HNFs under research are composed of the nanomolecules aluminum oxide (Al_2O_3), copper oxide (CuO), silver (Ag), and water (H_2O). In the current study, the novel combination Al_2O_3–CuO–Ag–H_2O was applied for the first time. This unique combination aids in environmental purification and the cooling of other appliances. Once the regulatory PDEs system has been transformed into linear ODEs utilizing the correspondence method, the robust KBM is employed to obtain numerical solutions. Tables and statistics displaying numerical results are utilizd to sustenance the observations. Entropy production has also been investigated for the modelled problem. It has been well addressed how particle morphologies are affected, as well as the convective slide boundary condition, current radiative movement, and smooth velocity.

Physical aspects and construction of system

In the cylindrical coordinate scheme (r,φ, z), we reflect an unstable magnetohydrodynamic (MHD) electrically guiding movement of THNFs through a stretchable turning floppy. As seen in Fig. 1, the disk switches with an angular velocity Ω while being positioned at z = 0 and laterally the z-axis. A fixed magnetic field, called B_0, is employed laterally the z-axis. It is supposed that the heat on the disk's shallow is $¥_\infty$, while the outside temperature is $¥_\infty$. Widening velocities, disk rotation, and temperature profiles all depend on both space and time.

To make the situation simpler, the following assumptions were made:

$$u = \frac{cr}{(1-bt)}, \quad v = \frac{c\Omega}{(1-bt)}, \quad B(t) = \frac{B_0}{\sqrt{(1-bt)}}, \quad ¥_s = ¥_0 - ¥_{Ref}\left(\frac{r^2\Omega}{v(1-bt)^{\frac{3}{2}}}\right). \quad (1)$$

The flow contains three different kinds of nanoparticles, including Ag, CuO, and Al_2O_3. It is anticipated that a sufficient strong magnetic field will influence the Hall movement. The full application of Ohm's law is as follows in the presence of an electric field:

$$J + \frac{\tau_e\omega_e}{B_0}(J \times B) = \sigma\mu_e(V \times B) + \frac{\sigma}{en_e}\nabla p_e, \quad (2)$$

assuming that for poorly ionized gas, the thermoelectric pressure and ion slideenvironments are unimportant. The aforesaid equations, in the following more condensed form:

$$J_r = \frac{\sigma\mu_e B_0}{1+m^2}(mv - u), J_\varphi = \frac{\sigma\mu_e B_0}{1+m^2}(mu + v), \quad (3)$$

where $c, b, \Omega, ¥_s, ¥_0, ¥_{ref}, \omega_e, \tau_e, Pe, n_e, \mu_e, m, \sigma, B_0, u$ an d v are the splayed quantity, progressive static quantity, disk rotating quantity, superficial thermal, source thermal, continual direction thermal, cyclotron incidence of
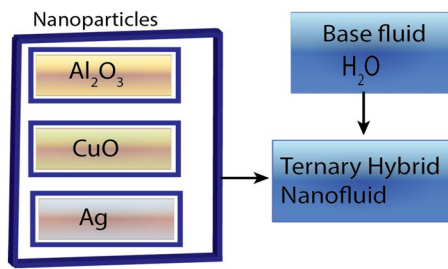
Figure 2. Organized attitude of tri-hybrid nanoparticles.

electrons, electron crash period, electron pressure, quantity of viscosity of electrons, magnetic permeability, Hall current bound, electrical conductivity of fluid, magnetic field influence, radiating and azimuthal velocities devices, correspondingly. The Hall factor is indicated here as $m = \tau_e \omega_e$, while liquid electrical conductivity is indicated as

$$\sigma = \frac{e^2 n_e t_e}{m_e}.$$ (4)

A flow diagram of the ternary hybrid nanoparticles TiO$_2$, Al$_2$O$_3$, and is shown in Fig. 2, with water (H$_2$O) being considered as an inappropriate fluid in the current issue.

Mathematical modeling system of eqautions

The representation figure in cylindrical coordinates (r, φ, z) for the continuous circling movement of the nanofluid through a stretchable and fixed disk is exposed in Fig. The rounded disk by means of fixed heat ($¥_s$) at $z = 0$ can be strained consistently in the radial direction by the side of an extending amount of (c). Henceforward, the leading calculations[87] of continuousness, momentum and dynamism are

$$\frac{1}{r}\frac{\partial}{\partial r}(ur) + \frac{\partial w}{\partial z} = 0,$$ (5)

$$\left(\frac{\partial u}{\partial t} - \frac{v^2}{r} + w\frac{\partial u}{\partial z} + u\frac{\partial u}{\partial r}\right) = v_{thnf}\left(\frac{\partial^2 u}{\partial z^2}\right) - \frac{\sigma_{thnf}B_0^2}{\rho_{thnf}(1 + ma^2)\sqrt{1-bt}}[u - mav],$$ (6)

$$\left(\frac{\partial v}{\partial t} + \frac{uv}{r} + u\frac{\partial v}{\partial r} + w\frac{\partial v}{\partial z}\right) = v_{thnf}\left(\frac{\partial^2 v}{\partial z^2}\right) - \frac{\sigma_{thnf}B_0^2}{\rho_{thnf}(1 + ma^2)\sqrt{1-bt}}[v + mau],$$ (7)

$$\left(\frac{\partial ¥}{\partial t} + u\frac{\partial ¥}{\partial r} + w\frac{\partial ¥}{\partial z}\right) = \frac{\kappa_{thnf}}{(\rho C_p)_{thnf}}\left(\frac{\partial^2 ¥}{\partial z^2}\right) + \frac{\mu_{thnf}}{(\rho C_p)_{thnf}}\left[\left(\frac{\partial u}{\partial z}\right)^2 - \left(\frac{\partial v}{\partial z}\right)^2\right] - \frac{1}{(\rho C_p)_{thnf}}\frac{\partial q_r}{\partial z}.$$ (8)

where $¥$, v_{thnf}, σ_{thnf}, ρ_{thnf}, κ_{thnf}, $(\rho C_p)_{thnf}$, and q_r are the liquefied temperature, kinematic viscosity, tri-HNF electrical directing, thickness of tri-HNF, current conductivity of tri-HNF, full heat of tri-HNF and radiative temperature fluidity. In this instance, the radiative temperature fluctuation may perhaps be situated via employing Rosseland estimate through incomes of:

$$q_r = -\frac{4\sigma^*}{3k^*}\frac{\partial ¥^4}{\partial Z} = -\frac{16\sigma^* ¥_\infty^3}{3k^*}\frac{\partial ¥}{\partial z},$$ (9)

Here, σ^* is the Boltzmann constant and k^* is the concentration number. In view of Eqs. (9) and (8), it can be communicated as

$$\left(\frac{\partial ¥}{\partial t} + u\frac{\partial ¥}{\partial r} + w\frac{\partial ¥}{\partial z}\right) = \frac{\kappa_{thnf}}{(\rho C_p)_{thnf}}\left(\frac{\partial^2 ¥}{\partial z^2}\right) + \frac{\mu_{thnf}}{(\rho C_p)_{thnf}}\left[\left(\frac{\partial u}{\partial z}\right)^2 - \left(\frac{\partial v}{\partial z}\right)^2\right] + \frac{16\sigma^* ¥_\infty^3}{(\rho C_p)_{thnf}3k^*}\frac{\partial^2 ¥}{\partial z^2}.$$ (10)

The relevant boundary conditions are:

$$\left.\begin{array}{l}(u, v, w, ¥) = \left(\frac{cr}{(1-bt)}, \frac{r\Omega}{(1-bt)}, 0, ¥_s\right) \quad \text{at } z = 0, \\ u = v = 0, ¥ \to ¥_\infty \quad as \; z \to \infty.\end{array}\right\}$$ (11)

The functioning attitude of tri-HNFs is the rearrangement of tri-various categories of nanoparticles in the improper fluid. This advances the TTcompetences of the normal fluids plus verifies a superior heat supporter

	K (thermal conductivity)	σ (electrical conductivity)	ρ (density)	C_p (heat capacity)
H_2O	0.613	0.05	997.1	4179
Al_2O_3	40	1×10^{-10}	3970	765
CuO	76.5	5.96×10^{7}	6320	531.5
Ag	429	3.60×10^{7}	10,500	235

Table 1. Thermal properties[89,90] of nanoparticles (Al_2O_3, CuO and Ag) in H_2O.

than the HNFs. Methodical expressions on the subject of the thermophysical properties for ternary HNF[88] arestated inferior to

$$\mu_{thnf} = \frac{\mu_f}{(1-\phi_1)^{2.5}(1-\phi_2)^{2.5}(1-\phi_3)^{2.5'}}$$

$$\rho_{thnf} = [(1-\phi_1)\{(1-\phi_2)[(1-\phi_3)\rho_f + \rho_3\phi_3] + \rho_2\phi_2\} + \rho_1\phi_1],$$

$$(\rho C_p)_{thnf} = (1-\phi_1)\{(1-\phi_2)[(1-\phi_3)(\rho C_p)_f + (\rho C_p)_3\phi_3] + (\rho C_p)_2\phi_2\} + (\rho C_p)_1\phi_1,$$

$$\frac{k_{thnf}}{k_{hnf}} = \frac{k_1 + 2k_{nf} - 2\phi_1(k_{nf}-k_1)}{k_1 + 2k_{nf} + \phi_1(k_{nf}-k_1)},$$

$$\frac{k_{hnf}}{k_{nf}} = \frac{k_2 + 2k_{nf} - 2\phi_2(k_{nf}-k_2)}{k_2 + 2k_{nf} + \phi_2(k_{nf}-k_2)},$$

$$\frac{k_{nf}}{k_f} = \frac{k_3 + 2k_{nf} - 2\phi_3(k_{nf}-k_3)}{k_3 + 2k_{nf} + \phi_3(k_{nf}-k_3)},$$

$$\frac{\sigma_{thnf}}{\sigma_{hnf}} = \frac{\sigma_1(1+2\phi_1) - \phi_{hnf}(1-2\phi_1)}{\sigma_1(1-\phi_1) + \sigma_{hnf}(1+\phi_1)}$$

$$\frac{\sigma_{hnf}}{\sigma_{nf}} = \frac{\sigma_2(1+2\phi_2) + \varphi_{nf}(1-2\phi_2)}{\sigma_2(1-\phi_2) + \sigma_{nf}(1+\phi_2)}$$

$$\frac{\sigma_{nf}}{\sigma_f} = \frac{\sigma_3(1+2\phi_3) + \varphi_f(1-2\phi_3)}{\sigma_3(1-\phi_3) + \sigma_f(1+\phi_3)}.$$

In which, μ_{thnf}, ρ_{thnf}, $\rho(C_p)_{thnf}$, κ and σ_f indicated the crescendos stickiness, thickness, specific temperature measurements of the THNFs thermal conductivity and electrical conductivity. $\phi = \phi_1 + \phi_2 + \phi_3$ is the nanoparticle capacity growth constant used at THNF and $\phi_1 = \phi_{Al_2O_3}$, $\phi_2 = \phi_{CuO}$, and $\phi_3 = \phi_{Ag}$ are the capacity fraction of the first, second, and third nanoparticles. μ_f, ρ_f, $(C_p)_f$, κ_f, σ_f and are self-motivatedviscidness, intensity, explicittemperaturecapability, current conductivity and electrical conductivity of the foundationliquid. $\rho_1, \rho_2, \rho_3, (C_p)_1, (C_p)_2, (C_p)_3, \kappa_1, \kappa_2, \kappa_3, \sigma_1, \sigma_2$ and σ_3 are the thicknesses, specific thermal measurements, thermal conductivities and electrical conductivitiesof the nanoparticles.

The physicalpossessions of the base liquidwaterand various nanoparticles being utilized in the existenttraining are illustrated in Table 1.

The result to the problem
Take into account the similarity transformations below:

$$u = \frac{r\Omega}{(1-bt)}F^{*'}, v = \frac{r\Omega}{(1-bt)}G^*, w = -2\sqrt{\frac{r\Omega}{(1-bt)}}F^*,$$

$$\chi = \sqrt{\frac{\Omega}{\nu(1-bt)}}z, \Upsilon = \Upsilon_0 - \Upsilon_{ref}\frac{\Omega r^2}{\nu(1-bt)^{\frac{3}{2}}}\theta^*. \qquad (12)$$

Aid to the above resemblance variables, Eqs. (4–7) and Eqs. (10, 11) are concentrated as:

$$\frac{D_1}{D_2}F^{*'''} + (G^{*2} + 2F^*F^{*''} - (F^{*'})^2) - A^*(\frac{\chi}{2}F^{*''} + F^{*'}) - \frac{D_3}{D_2(1+ma^2)}Ha(F^{*'} - maG^*) = 0, \qquad (13)$$

$$\frac{D_1}{D_2}G^{*''} - 2(F^*G^{*'} - G^*F^{*'}) - A^*(\frac{\chi}{2}G^{*'} + G^*) - \frac{D_3}{D_2(1+ma^2)}Ha(G^* - maG^{*'}) = 0, \qquad (14)$$

$$D_4\left(D_5 + \frac{4}{3}Nr\right)\theta^{*''} + PrA^*\left(\frac{\chi}{2}\theta^{*'} + \frac{3}{2}\theta^*\right) + 2Pr(F\theta^{*'} - F^{*'}\theta^*) - \frac{D_4}{D_1}Prhc\left((F^{*''})^2 + (G^{*'})^2\right) = 0, \qquad (15)$$

with conditions

$$F^*(0) = 0, F^{*'}(0) = \omega, \theta^*(0) = 1 = G^*(0) \quad \text{at } \chi = 0$$
$$F^{*'}(\chi) = 0, G^*(\chi) \to 0, \theta^*(\chi) \to 0, \quad as \ \chi \to \infty \qquad (16)$$

where ω, A^*, Ha, ma, Nr, Pr, and hc are rotation parameter, the quantity of trembling, magnetic field aspect, Hallcurrent factor, radiation aspect, Prandtl number and Eckert number, correspondingly. These uni-dimensional limitations and measured forms of the coefficients.
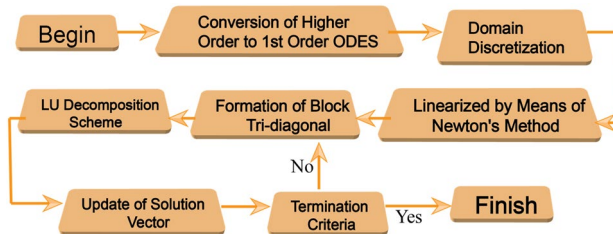
Figure 3. Current diagram demonstrating the Keller box technique.

D_1, D_2, D_3, D_4 and D_5 can be expressed as:

$$D_1 = \frac{\mu_{thnf}}{\mu_f}, D_2 = \frac{\rho_{thnf}}{\rho_f}, D_3 = \frac{\sigma_{thnf}}{\sigma_f}, D_4 = \frac{(\rho C_p)_f}{(\rho C_p)_{thnf}},$$
$$D_5 = \frac{\kappa_{thnf}}{\kappa_f}, \omega = \frac{\Omega}{c}, A^* = \frac{b}{\Omega}, Ha = \frac{\sigma_f B_0^2}{\rho_f \Omega}, ma = \omega_e$$
$$Nr = \frac{4\sigma^* \Psi_\infty^3}{\kappa^* \kappa_f}, Pr = \frac{\mu_f (\rho C_p)_f}{\rho_f \kappa_f}, hc = \frac{r^2 \Omega^2}{(1-bt)^2 C_s} \tag{17}$$

Skin friction and Nusselt number. Skin friction and Nusselt number are fairly appreciated for manufacturing purposes at the nano-level. The present somatic problem skin friction, is formulated by:

$$\mathrm{Re}^{\frac{1}{2}} Cf_r = \frac{F''(0)}{(1 - \phi_1)^{2.5}(1 - \phi_2)^{2.5}(1 - \phi_3)^{2.5}} \tag{18}$$

$$\mathrm{Re}^{\frac{1}{2}} Cg_r = \frac{G'(0)}{(1 - \phi_1)^{2.5}(1 - \phi_2)^{2.5}(1 - \phi_3)^{2.5}} \tag{19}$$

and Nusselt number is given by

$$Nu_r \mathrm{Re}^{-\frac{1}{2}} = -\frac{\kappa_{thnf}}{\kappa_f}\left(1 + \frac{4}{3}Nr\right)\theta^{*'}(0), \tag{20}$$

where $Re = \frac{r^2 \Omega}{\nu_f(1-bt)}$ is the Reynolds number.

Entropy generation analysis
The data presented by Bejan[94] are used to formulate the volumetric entropy generation rate with the effects of TT and liquid friction

$$E = \frac{1}{\Psi^2}\left(\kappa_{thnf} + \frac{16}{3}\frac{\sigma^* \Psi_0^3}{\kappa^*}\right)\left(\frac{\partial \Psi}{\partial z}\right)^2 + \frac{\mu_{thnf}}{\Psi_0}\left(\left(\frac{\partial u}{\partial z}\right)^2 + \left(\frac{\partial v}{\partial z}\right)^2\right) + \frac{\sigma_{thnf} B_0^2 (u^2 + v^2)}{k\Psi_0(1 + ma^2)(1 - bt)}. \tag{21}$$

The reduced entropy generation equation is as follows:

$$N_G = \alpha_a\left(D_5 + \frac{4}{3}Nr\right)\theta^{*'2} + D_1 Br\left(F^{*''2} + G^{*'2}\right) + \frac{D_3 MBr}{(1 + ma^2)\left(F^{*'2} + G^{*2}\right)}. \tag{22}$$

Here $\alpha_a = \frac{\Delta\Psi}{\Psi_0}$ is the dimensionless temperature difference, in which $\Delta\Psi = \Psi_{ref}\left(\frac{r^2\Omega}{\nu(1-bt)^{\frac{3}{2}}}\right), Br = \frac{\mu_f r^2 \Omega^2}{k_f(\Psi_w - \Psi_\infty)}$ is the Brinkman number, $\omega = \frac{\Psi_w - \Psi_\infty}{\Psi_\infty}$ is the dimensionless temperature gradient and $N_G = \left(\frac{\Psi_0 E_G \nu(1-bt)}{\kappa_f \Omega \Delta\Psi}\right)$ is the entropy generation rate.

Numerical implementation
Here, the Keller box technique[92,93] is utilized using the algebraic database Matlab for different principles of the relevant parameters to address the nonlinear ordinary differential Eqs. (14)–(16) with respect to the endpoint condition (Eq. 17). Despite recent advances in other numerical approaches, this method appears to be the most flexible of the popular methods and remains a powerful and extremely accurate solution for parabolic boundary layer flows. It can also solve equations of any order and is absolutely stable on the results. The flow process chart (see Fig. 3) represents the step-by-step Keller box scheme procedure as follows:

Adaptation of ODEs. We begin by including renewed independent variables: $\xi_1(x, \chi), \xi_2(x, \chi), \xi_3(x, \chi), \xi_4(x, \chi), \xi_5(x, \chi), \xi_6(x, \chi)$ and $\xi_7(x, \chi)$ with $\xi_1 = F^*, \xi_2 = F^{*'}, \xi_3 = F^{*''}, \xi_4 = G, \xi_5 = G^*, \xi_6 = \theta^*$ and $\xi_7 = \theta^{*'}$. This transformation causes Eqs. (10–12) to decrease to the subsequent first-order formula
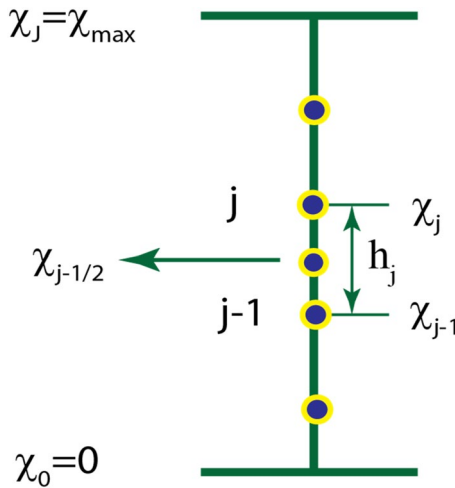
Figure 4. Representative grid structure for modification evaluations.

$$\frac{d\xi_1}{d\chi} = \xi_2, \tag{23}$$

$$\frac{d\xi_2}{d\chi} = \xi_3, \tag{24}$$

$$\frac{d\xi_4}{d\chi} = \xi_5, \tag{25}$$

$$\frac{d\xi_6}{d\chi} = \xi_7, \tag{26}$$

$$\frac{D_1}{D_2}\frac{d\xi_3}{d\chi} + (\xi_4 - 2\xi_1\xi_3 - \xi_2^2) - A^*\left(\frac{\chi}{2}\xi_3 + \xi_2\right) - \frac{D_3}{D_2(1+ma^2)}Ha(\xi_2 - ma\xi_4) = 0, \tag{27}$$

$$\frac{D_1}{D_2}\frac{d\xi_5}{d\chi} - 2(\xi_1\xi_5 - \xi_2\xi_4) - A^*\left(\frac{\chi}{2}\xi_5 + \xi_4\right) - \frac{D_3}{D_2(1+ma^2)}Ha(\xi_4 - ma\xi_2) = 0, \tag{28}$$

$$\left.\begin{array}{l} D_4\left(D_5 + \frac{4}{3}Nr\right)\frac{d\xi_7}{d\chi} - PrA^*\left(\frac{\chi}{2}\xi_7 + \frac{3}{2}\xi_6\right) + 2Pr(\xi_1\xi_7 - \xi_2\xi_6) \\ -\frac{D_4}{D_1}Prhc\left(\xi_3^2 + \xi_5^2\right) = 0, \end{array}\right\} \tag{29}$$

$$\left.\begin{array}{l} \xi_1(0) = 0, \xi_2(0) = \omega, \xi_4(0) = 1 = \xi_6(0) \quad \text{at } \chi = 0 \\ \xi_2(\chi) = 0, \xi_4(\chi) \to 0, \xi_6(\chi) \to 0, \quad as \ \chi \to \infty \end{array}\right\} \tag{30}$$

Dominiondiscretization and difference equations. Additionally, area discretization in $x - \chi$ plane is characterized in Fig. 4. According to this arguments, we have

$\chi_0 = 0, \chi_j = \chi_{j-1} + h_j, j = 0, 1, 2, 3..., J, \chi_J = 1$ where, h_j is the step-magnitude. Applying central difference construction at the midpoint $\chi_{j-0.5}$

Employing the central difference preparation at the medium point $\xi_{j-1/2}$

$$(\xi_1)_j - (\xi_1)_{j-1} = 0.5 * h_j((\xi_2)_j + (\xi_2)_{j-1}), \tag{31}$$

$$(\xi_2)_j - (\xi_2)_{j-1} = 0.5 * h_j((\xi_3)_j + (\xi_3)_{j-1}), \tag{32}$$

$$(\xi_4)_j - (\xi_4)_{j-1} = 0.5 * h_j((\xi_5)_j + (\xi_5)_{j-1}), \tag{33}$$

$$(\xi_6)_j - (\xi_6)_{j-1} = 0.5 * h_j((\xi_7)_j + (\xi_7)_{j-1}), \tag{34}$$

8

$$\left.\begin{array}{l} \frac{D_1}{D_2}\frac{((\xi_3)_j-(\xi_3)_{j-1})}{h_j} + \left(\frac{\left(\frac{(\xi_4)_j+(\xi_4)_{j-1}}{2}\right)^2}{4}\right. \\ +2\times\left(\frac{(\xi_1)_j+(\xi_1)_{j-1}}{2}\right)\left(\frac{(\xi_3)_j+(\xi_3)_{j-1}}{2}\right)-\left.\left(\frac{(\xi_2)_j+(\xi_2)_{j-1}}{2}\right)^2\right) \\ -A^*\left(\frac{\chi}{2}\left(\frac{(\xi_3)_j+(\xi_3)_{j-1}}{2}\right)+\left(\frac{(\xi_2)_j+(\xi_2)_{j-1}}{2}\right)\right) \\ -\frac{D_3}{D_2(1+ma^2)}Ha\left(\left(\frac{(\xi_2)_j+(\xi_2)_{j-1}}{2}\right)-ma\left(\frac{(\xi_4)_j+(\xi_2)_{j-1}}{4}\right)\right)=0, \end{array}\right\} \tag{35}$$

$$\left.\begin{array}{l} \frac{D_1}{D_2}\frac{((\xi_5)_j-(\xi_5)_{j-1})}{h_j} - 2\left(\left(\frac{(\xi_1)_j+(\xi_1)_{j-1}}{2}\right)\left(\frac{(\xi_5)_j+(\xi_5)_{j-1}}{2}\right)-\left(\frac{(\xi_2)_j+(\xi_2)_{j-1}}{2}\right)\right. \\ \left.\left(\frac{(\xi_4)_j+(\xi_4)_{j-1}}{2}\right)\right)-A^*\left(\frac{\chi}{2}\left(\frac{(\xi_5)_j+(\xi_5)_{j-1}}{2}\right)+\left(\frac{(\xi_4)_j+(\xi_4)_{j-1}}{2}\right)\right) \\ -\frac{D_3}{D_2(1+ma^2)}Ha\left(\left(\frac{(\xi_4)_j+(\xi_4)_{j-1}}{2}\right)-ma\left(\frac{(\xi_2)_j+(\xi_2)_{j-1}}{2}\right)\right)=0, \end{array}\right\} \tag{36}$$

$$\left.\begin{array}{l} D_4\left(D_5+\frac{4}{3}Nr\right)\frac{((\xi_7)_j-(\xi_7)_{j-1})}{h_j}-PrA^*\left(\frac{\chi}{2}\left(\frac{(\xi_7)_j+(\xi_7)_{j-1}}{2}\right)+\frac{3}{2}\left(\frac{(\xi_6)_j+(\xi_6)_{j-1}}{2}\right)\right) \\ +2Pr\left(\left(\frac{(\xi_1)_j+(\xi_1)_{j-1}}{2}\right)\left(\frac{(\xi_7)_j+(\xi_7)_{j-1}}{2}\right)-\left(\frac{(\xi_2)_j+(\xi_2)_{j-1}}{2}\right)\left(\frac{(\xi_6)_j+(\xi_6)_{j-1}}{2}\right)\right) \\ -\frac{D_4}{D_1}Prhc\left(\left(\frac{(\xi_3)_j+(\xi_3)_{j-1}}{2}\right)^2+\left(\frac{(\xi_5)_j+(\xi_5)_{j-1}}{2}\right)^2\right)=0, \end{array}\right\} \tag{37}$$

Newton technique. The Newton linearization method is used to linearize Eqs. (28)–(34) in this formula.

$$\left.\begin{array}{l} (\xi_1)_j^{m+1}=(\xi_1)_j^m+(\delta\xi_1)_j^m,(\xi_2)_j^{m+1}=(\xi_2)_j^m+(\delta\xi_2)_j^m, \\ (\xi_3)_j^{m+1}=(\xi_3)_j^m+(\delta\xi_3)_j^m,(\xi_4)_j^{m+1}=(\xi_4)_j^m+(\delta\xi_4)_j^m, \\ (\xi_5)_j^{m+1}=(\xi_5)_j^m+(\delta\xi_5)_j^m,(\xi_6)_j^{m+1}=(\xi_6)_j^m+(\delta\xi_6)_j^m, \\ (\xi_7)_j^{m+1}=(\xi_7)_j^m+(\delta\xi_7)_j^m. \end{array}\right\} \tag{38}$$

The resulting set of equations is generated by substituting the expressions found in Eqs. (28) via (34) and reducing the square and upper powers of.

$$((\delta\xi_1)_j-(\delta\xi_1)_{j-1})-0.5*h_j((\delta\xi_2)_j+(\delta\xi_2)_{j-1})=(r_1)_j, \tag{39}$$

$$((\delta\xi_2)_j-(\delta\xi_2)_{j-1})-0.5*h_j((\delta\xi_3)_j+(\delta\xi_3)_{j-1})=(r_2)_j, \tag{40}$$

$$((\delta\xi_4)_j-(\delta\xi_4)_{j-1})-0.5*h_j((\delta\xi_5)_j+(\delta\xi_5)_{j-1})=(r_3)_j, \tag{41}$$

$$((\delta\xi_6)_j-(\delta\xi_6)_{j-1})-0.5*h_j((\delta\xi_7)_j+(\delta\xi_7)_{j-1})=(r_4)_j, \tag{42}$$

$$\left.\begin{array}{l} (C_1)_j(\delta\xi_1)_j+(C_2)_j(\delta\xi_1)_{j-1}+(C_3)_j(\delta\xi_2)_j+(C_4)_j(\delta\xi_2)_{j-1}+(C_5)_j(\delta\xi_3)_j \\ +(C_6)_j(\delta\xi_3)_{j-1}+(C_7)_j(\delta\xi_4)_j+(C_8)_j(\delta\xi_4)_{j-1}=(r_5)_j, \end{array}\right\} \tag{43}$$

$$\left.\begin{array}{l} (D_1)_j(\delta\xi_1)_j+(D_2)_j(\delta\xi_1)_{j-1}+(D_3)_j(\delta\xi_2)_j+(D_4)_j(\delta\xi_2)_{j-1}+(D_5)_j(\delta\xi_4)_j \\ +(D_6)_j(\delta\xi_4)_{j-1}+(D_7)_j(\delta\xi_5)_j+(D_8)_j(\delta\xi_5)_{j-1}=(r_6)_j, \end{array}\right\} \tag{44}$$

$$\left.\begin{array}{l} (E_1)_j(\delta\xi_1)_j+(E_2)_j(\delta\xi_1)_{j-1}+(E_3)_j(\delta\xi_2)_j+(E_4)_j(\delta\xi_2)_{j-1}+(E_5)_j(\delta\xi_3)_j \\ +(E_6)_j(\delta\xi_3)_{j-1}+(E_7)_j(\delta\xi_5)_j+(E_8)_j(\delta\xi_5)_{j-1}+(E_9)_j(\delta\xi_6)_j+(E_{10})_j(\delta\xi_6)_{j-1} \\ +(E_{11})_j(\delta\xi_7)_j+(E_{12})_j(\delta\xi_7)_{j-1}=(r_7)_j, \end{array}\right\} \tag{45}$$

where

$$\left.\begin{array}{l} (C_1)_j=2h_j\left(\frac{(\xi_3)_j+(\xi_3)_{j-1}}{4}\right)=(C_2)_j, \\ (C_3)_j=-\frac{\delta LS}{2}-h_j\left(\frac{(\xi_2)_j+(\xi_2)_{j-1}}{2}\right)-\frac{h_jMB_3}{2B_2(1+ma^2)}=(C_4)_j, \\ (C_5)_j=-\frac{h_jA^*\xi}{4}+\frac{D_1}{D_2}+2\delta L\left(\frac{(\xi_1)_j+(\xi_1)_{j-1}}{4}\right), \\ (C_6)_j=-\frac{h_jA^*\xi}{4}-\frac{D_1}{D_2}+2\delta L\left(\frac{(\xi_1)_j+(\xi_1)_{j-1}}{4}\right), \\ (C_7)_j=h_j\left(\frac{(\xi_4)_j+(\xi_4)_{j-1}}{2}\right)+\frac{h_jmMB_3}{2B_2(1+ma^2)}=(C_8)_j, \end{array}\right\} \tag{46}$$

$$(r_5)_j = -\frac{D_1}{D_2}\frac{((\xi_3)_j - (\xi_3)_{j-1})}{h_j} - \left(\frac{((\xi_4)_j + (\xi_4)_{j-1})^2}{4}\right.$$
$$\left. -2\left(\frac{(\xi_1)_j + (\xi_1)_{j-1}}{2}\right)\left(\frac{(\xi_3)_j + (\xi_3)_{j-1}}{2}\right) + \left(\frac{(\xi_2)_j + (\xi_2)_{j-1}}{2}\right)^2\right)$$
$$+ A^*\left(\frac{\chi}{2}\left(\frac{(\xi_3)_j + (\xi_3)_{j-1}}{2}\right) + \left(\frac{(\xi_2)_j + (\xi_2)_{j-1}}{2}\right)\right)$$
$$+ \frac{D_3}{D_2(1+ma^2)}Ha\left(\left(\frac{(\xi_2)_j + (\xi_2)_{j-1}}{2}\right) + ma\left(\frac{(\xi_4)_j + (\xi_2)_{j-1}}{4}\right)\right), \tag{47}$$

$$(D_1)_j = 2h_j\left(\frac{(\xi_5)_j + (\xi_5)_{j-1}}{4}\right) = (D_2)_j,$$
$$(D_3)_j = 2h_j\left(\frac{(\xi_4)_j + (\xi_4)_{j-1}}{4}\right) - \frac{h_j MB_3}{2B_2(1+ma^2)} = (D_4)_j,$$
$$(D_5)_j = -\frac{h_j A^*}{2} - \frac{h_j A^*\xi}{4} + 2h_j\left(\frac{(\xi_2)_j + (\xi_2)_{j-1}}{4}\right) + \frac{h_j mMB_3}{2B_2(1+ma^2)} = (D_6)_j,$$
$$(D_7)_j = -\frac{h_j}{2} + \frac{D_1}{D_2} - 2h_j\left(\frac{(\xi_1)_j + (\xi_1)_{j-1}}{4}\right),$$
$$(D_8)_j = -\frac{h_j}{2} - \frac{D_1}{D_2} - 2h_j\left(\frac{(\xi_1)_j + (\xi_1)_{j-1}}{4}\right), \tag{48}$$

$$(r_6)_j = -\frac{D_1}{D_2}\frac{((\xi_5)_j - (\xi_5)_{j-1})}{h_j} + 2\left(\left(\frac{(\xi_1)_j + (\xi_1)_{j-1}}{2}\right)\left(\frac{(\xi_5)_j + (\xi_5)_{j-1}}{2}\right)\right.$$
$$\left. -\left(\frac{(\xi_2)_j + (\xi_2)_{j-1}}{2}\right)\left(\frac{(\xi_4)_j + (\xi_4)_{j-1}}{2}\right)\right) + A^*\frac{\chi}{2}\left(\frac{(\xi_5)_j + (\xi_5)_{j-1}}{2}\right)$$
$$+ A^*\left(\frac{(\xi_4)_j + (\xi_4)_{j-1}}{2}\right) + \frac{D_3}{D_2(1+ma^2)}Ha\left(\left(\frac{(\xi_4)_j + (\xi_4)_{j-1}}{2}\right) + ma\left(\frac{(\xi_2)_j + (\xi_2)_{j-1}}{2}\right)\right), \tag{49}$$

$$(E_1)_j = 2h_j Pr\left(\frac{(\xi_7)_j + (\xi_7)_{j-1}}{4}\right) = (E_2)_j,$$
$$(E_3)_j = -2h_j Pr\left(\frac{(\xi_6)_j + (\xi_6)_{j-1}}{4}\right),$$
$$(E_5)_j = -\frac{hch_j PrB_4}{2B_1} = (E_6)_j,$$
$$(E_7)_j = -\frac{hch_j PrB_4}{2B_1} = (E_8)_j,$$
$$(E_9)_j = -\frac{3}{4}h_j Pr A^* - 2h_j Pr\left(\frac{(\xi_2)_j + (\xi_2)_{j-1}}{4}\right) = (E_{10})_j,$$
$$(E_{11})_j = -\frac{1}{4}h_j nPr - D_4(D_5 + 4/3Rd) + 2h_j Pr\left(\frac{(\xi_1)_j + (\xi_1)_{j-1}}{4}\right),$$
$$(E_{12})_j = \frac{1}{4}h_j nPr - D_4(D_5 + 4/3Rd) + 2h_j Pr\left(\frac{(\xi_1)_j + (\xi_1)_{j-1}}{4}\right), \tag{50}$$

$$(r_7)_j = -D_4\left(D_5 + \frac{4}{3}Nr\right)\frac{((\xi_7)_j - (\xi_7)_{j-1})}{h_j}$$
$$+ Pr\, A*\left(\frac{\chi}{2}\left(\frac{(\xi_7)_j + (\xi_7)_{j-1}}{2}\right) + \frac{3}{2}\left(\frac{(\xi_6)_j + (\xi_6)_{j-1}}{2}\right)\right)$$
$$-2\, Pr\left(\frac{(\xi_1)_j + (\xi_1)_{j-1}}{2}\right)\left(\frac{(\xi_7)_j + (\xi_7)_{j-1}}{2}\right)$$
$$+2\, Pr\left(\frac{(\xi_2)_j + (\xi_2)_{j-1}}{2}\right)\left(\frac{(\xi_6)_j + (\xi_6)_{j-1}}{2}\right)$$
$$+ \frac{D_4}{D_1} Pr\, hc\left(\left(\frac{(\xi_3)_j + (\xi_3)_{j-1}}{2}\right)^2 + \left(\frac{(\xi_5)_j + (\xi_5)_{j-1}}{2}\right)^2\right). \tag{51}$$

Block tridiagonal structure. The linearized scheme's subsequent block tridiagonal construction is as follows.

$$A\Delta = S, \tag{52}$$

where

$$A = \begin{bmatrix} [A_1^*] & [C_1^*] \\ [A_2^*] & [C_2^*] \\ & & \ddots \\ & & & \ddots \\ & & & & \ddots \\ & & & & [B_{J-1}^*] & [A_{J-1}^*] & [C_{J-1}^*] \\ & & & & & [B_J^*] & [A_J^*] \end{bmatrix}, \quad \Delta = \begin{bmatrix} [\Delta_1] \\ [\Delta_2] \\ \vdots \\ \vdots \\ \vdots \\ [\Delta_{J-1}] \\ [\Delta_J] \end{bmatrix} \text{ and } S = \begin{bmatrix} [S_1] \\ [S_2] \\ \vdots \\ \vdots \\ \vdots \\ [S_{J-1}] \\ [S_J] \end{bmatrix}.$$

where the features demarcated in Eq. (52) be situated, as follows:

	Bachok et al.[94]	Turkyilmazoglu[95]	Proposed method
$F^{*\prime}(0)$	1.3582	1.35820634	1.3582063363
$-G^{*\prime}(0)$	0.9174	0.91688455	0.9168344188
$-\theta^{*\prime}(0)$	4.7573	4.75693830	4.7568976786

Table 2. A comparison of the $F^{*\prime}(0)$, $-G^{*\prime}(0)$ and $-\theta^{*\prime}(0)$ on static $Pr = 6.2$ through Refs.[94,95].

$$[A_1^*] = \begin{bmatrix} 0 & 0 & 0 & 1 & 0 & 0 & 0 \\ -0.5*h_j & 0 & 0 & 0 & -0.5*h_j & 0 & 0 \\ 0 & -0.5*h_j & 0 & 0 & 0 & -0.5*h_j & 0 \\ 0 & 0 & -0.5*h_j & 0 & 0 & 0 & -0.5*h_j \\ (C_6)_1 & 0 & 0 & (C_1)_1 & (C_5)_1 & 0 & 0 \\ 0 & (D_8)_1 & 0 & (D_1)_1 & 0 & (D_7)_1 & 0 \\ (E_6)_1 & (E_8)_1 & (E_{12})_1 & (E_1)_1 & (E_5)_1 & (E_7)_1 & (E_{11})_1 \end{bmatrix},$$

$$[A_j^*] = \begin{bmatrix} -0.5*h_j & 0 & 0 & 1 & 0 & 0 & \\ -1 & 0 & 0 & 0 & -0.5*h_j & 0 & 0 \\ 0 & -1 & 0 & 0 & 0 & -0.5*h_j & 0 \\ 0 & 0 & -1 & 0 & 0 & & -0.5*h_j \\ (C_4)_j & (C_8)_j & 0 & (C_1)_j & (C_5)_j & 0 & 0 \\ (D_4)_j & (D_6)_j & 0 & (D_1)_j & 0 & (D_7)_j & 0 \\ (E_4)_j & 0 & (E_{10})_j & (E_1)_j & (E_5)_j & (E_7)_j & (E_{11})_j \end{bmatrix}, 2 \leq j \leq J$$

$$[B_j^*] = \begin{bmatrix} 0 & 0 & 0 & -1 & 0 & 0 & 0 \\ 0 & 0 & 0 & 0 & -0.5*h_j & 0 & 0 \\ 0 & 0 & 0 & 0 & 0 & -0.5*h_j & 0 \\ 0 & 0 & 0 & 0 & 0 & 0 & -0.5*h_j \\ 0 & 0 & 0 & (C_3)_j & 0 & 0 & 0 \\ 0 & 0 & 0 & (D_2)_j & 0 & (D_8)_j & 0 \\ 0 & 0 & 0 & (E_2)_j & (E_6)_j & (E_8)_j & (E_{12})_j \end{bmatrix}, 2 \leq j \leq J$$

$$[C_j^*] = \begin{bmatrix} -0.5*h_j & 0 & 0 & 0 & 0 & 0 & 0 \\ 1 & 0 & 0 & 0 & 0 & 0 & 0 \\ 0 & 1 & 0 & 0 & 0 & 0 & 0 \\ 0 & 0 & 1 & 0 & 0 & 0 & 0 \\ (C_3)_j & (C_7)_j & 0 & 0 & 0 & 0 & 0 \\ (D_3)_j & (D_5)_j & 0 & 0 & 0 & 0 & 0 \\ (E_3)_j & 0 & (E_9)_j & 0 & 0 & 0 & 0 \end{bmatrix}, 1 \leq j \leq J-1.$$

Currently, the factorization of A can be viewed as follows:

$$A = LU, \tag{53}$$

where

$$L = \begin{bmatrix} [\Gamma_1^*] & & & & \\ & [\Gamma_2^*] & & & \\ & & \ddots & & \\ & & & \ddots & [\Gamma_{J-1}^*] & \\ & & & & [B_J^*] & [\Gamma_J^*] \end{bmatrix}, U = \begin{bmatrix} [I] & [\alpha_1^*] & & & \\ & [I] & [\alpha_2^*] & & \\ & & \ddots & \ddots & \\ & & & [I] & [\alpha_{J-1}^*] \\ & & & & [I] \end{bmatrix},$$

where the entire magnitude of matrix A is $J \times J$ by means of all block magnitude of super-vectors actually 7×7 plus $[I], [\Gamma_i^*]$ and $[\alpha_i^*]$ are the matrices of degree 7. Applying LU decomposition procedure aimed at the resolution of Δ. Aimed at scientific valuation, a netting magnitude of $\Delta h_j = 0.01$ is presumed obtainable to remain suitable, and the consequences remain assimilated consuming an error broadmindedness of 10^{-6}.

Cryptogram authentication. It is noted that the results of the current study are approximations based on the Keller box approach. Table 2 provides a summary of the results' coherence with relation to results from earlier methodologies. In the absence of the unsteadiness parameter, Hall current parameter, magnetic parameter, radiation parameter, Prandtl number parameter, and Eckert number parameter presented in Table 3, a comparison table is created. Table 3 shows numerical value comparisons between the present literature and those

		Nanofluid		Hybrid nanoparticles		Tri-hybrid nanoparticles	
		$\sqrt{R_e}Cf_r$	$\sqrt{R_e}Cg_r$	$\sqrt{R_e}Cf_r$	$\sqrt{R_e}Cg_r$	$\sqrt{R_e}Cf_r$	$\sqrt{R_e}Cg_r$
ϕ	0.01	1.70874	0.96380	1.72329	0.97587	1.72857	0.97699
	0.02	1.85219	0.96659	1.93863	1.04194	2.00093	1.06106
	0.03	1.97949	0.97142	2.21862	1.13243	2.34354	1.17800
A^*	0.5	0.04781	−1.09216	1.60144	0.44374	0.34858	−1.13744
	1.5	1.85219	0.96659	2.02912	1.07071	2.34354	1.17800
	2.5	2.14496	1.37184	2.34495	1.50717	2.73295	1.71961
ma	1	1.85219	0.96659	2.02912	1.07071	2.34354	1.17800
	2	1.54681	0.63189	1.69023	0.69950	1.97309	0.77157
	3	1.21246	0.23650	1.31689	0.25860	1.57192	0.29677
Ha	0.5	1.32548	0.24375	1.44335	0.26721	1.70692	0.30531
	1	1.42653	0.38053	1.55629	0.42000	1.82815	0.46866
	1.5	1.55392	0.55562	1.69808	0.61488	1.98183	0.67925
ω	0.4	0.45287	1.42276	0.49955	1.56456	0.55997	1.77762
	0.8	1.35389	1.11564	1.48475	1.23212	1.70724	1.37376
	1.2	2.38047	0.82053	2.60598	0.91251	3.01910	0.98633

Table 3. Comparison models among NFs, HNFs and tri-HNFs of skin frictions.
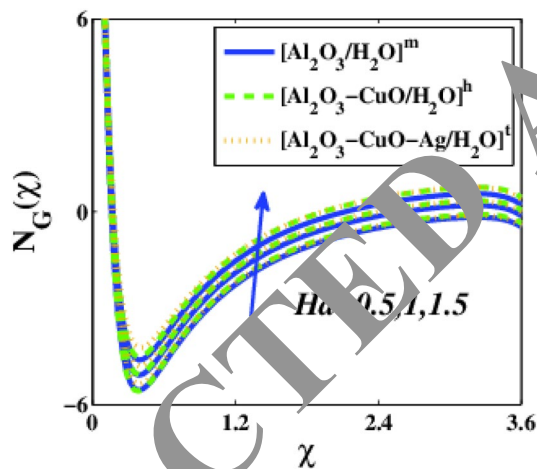
Figure 5. Conclusion of Ha on $N_G(\chi)$.
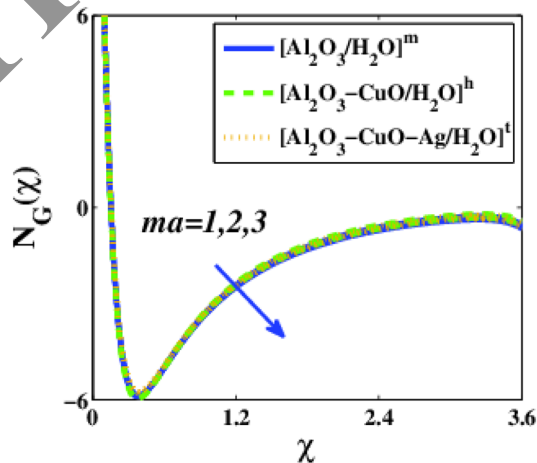
Figure 6. Influence of ma on $N_G(\chi)$.
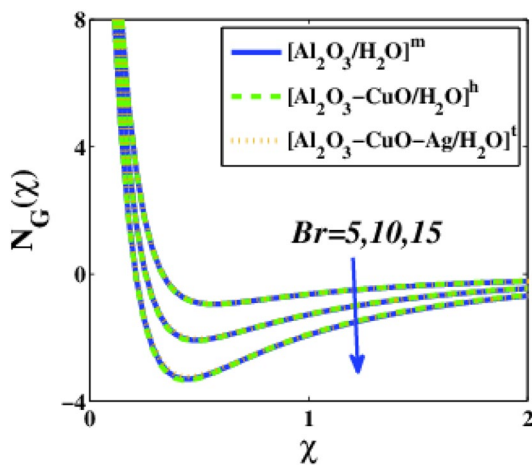
Figure 7. Impression of Br on $N_G(\chi)$.
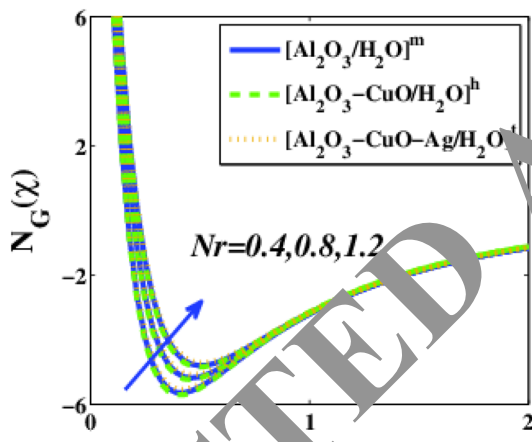
Figure 8. Control of Nr on $N_G(\chi)$.

of chok et al.[94] and Turkyilmazoglu[95]. The table shows that the current study has been compared and that the results are quite dependable.

Outcomes and discussion

The possessions of the factors corresponding to magnetic field parameter Ha, Hall current parameter ma, Brinkman number Br, Radiation parameter Nr, rotation parameter ω, solid volume fraction parameters ϕ_1, ϕ_2, ϕ_3, Prandtl number Pr, Eckert number hc, and measure of unsteadiness parameter A^* on the dimensionless profiles of Entropy $N_G(\chi)$, velocity components $\left(F'^*(\chi), G^*(\chi)\right)$ and temperature $\theta^*(\chi)$ are analyzed in this section. In order to produce results in the form of figures and tables, the parameter values must be between $0.5 \leq Ha \leq 1.5$, $1 \leq ma \leq 3, 5 \leq Br \leq 15, 0.4 \leq Nr \leq 1.2, 0.4 \leq \omega \leq 1.5, 0.01 \leq \phi \leq 0.03, 0.5 \leq A^* \leq 2.5, 0.5 \leq hc \leq 2.5$ and $5 \leq Pr \leq 7$.

The entropy profile $N_G(\chi)$ in Fig. 5 is decaying for growing estimations of the magnetic parameter Ha. When Ha is higher, the resistive Lorentzian force is formed, slowing the fluid velocity. Furthermore, when a stronger magnetic field is present, the temperature rises owing to Ohmic heating, resulting in the input of considerable heat. As a consequence, Entropy increases. The entropy profile $N_G(\chi)$ decreases in Fig. 6 for larger Hall current parameter ma. The decreasing effects look similar for all nanoparticles. The escalation in Brinkmann's number causes a decrease in Entropy (see Fig. 7). It is emphasised that the parameter Br contributes to fluid erosion in the dissipative flow pattern. Upon increasing the radiation parameter, the entropy production escalates along χ in Fig. 8. It is because of rising emissions, which raise frictional irreversibility and promote entropy production.

The consequences of the magnetic parameter Ha on the velocity components (radial $F'^*(\chi)$ and azimuthal $G^*(\chi)$)and temperature $\theta^*(\chi)$ are displayed in Figs. 9, 10 and 11. It is experienced both components are decaying
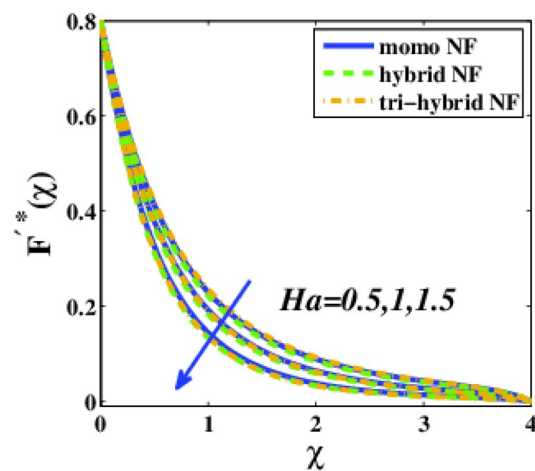
Figure 9. Inspiration of Ha on $F^{*'}(\chi)$.
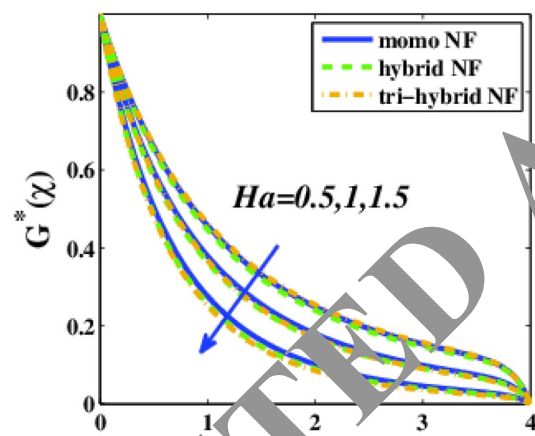

Figure 10. Impression of Ha on $G^*(\chi)$.
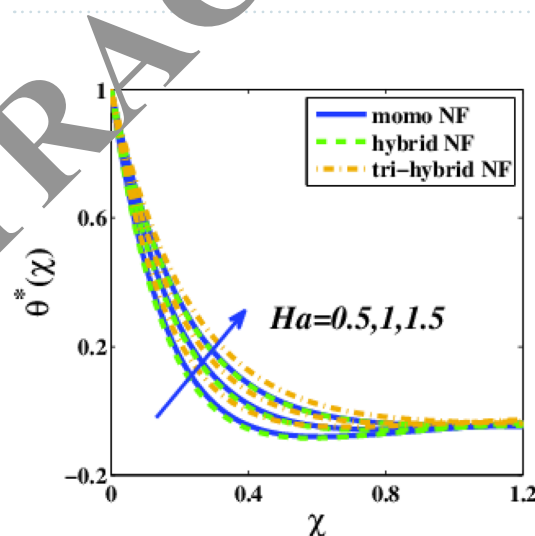
**Figure 11.** Effect of Ha on $\theta^*(\chi)$.
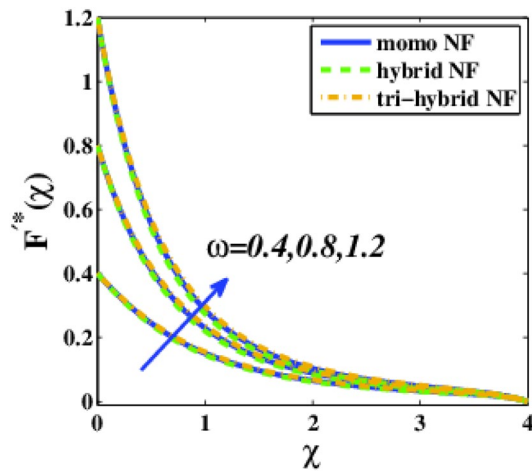
**Figure 12.** Control of ω on $F^{*'}(\chi)$.

Figure 13. Power of ω or $G^{*}(\chi)$.
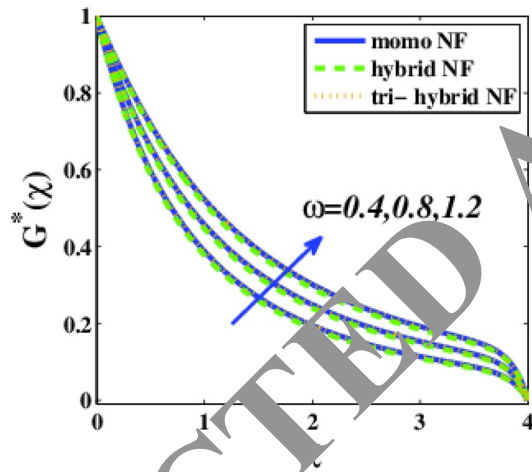
along χ whereas as temperature escalates for diverse estimations of the parameter Ha. As the magnetic parameter grows, the thickness of the velocity boundary layer rises. This occurs because the Lorentz force is put in motion in the transverse magnetic field, which causes a retarding force to act on the velocity field. As a consequence, the retarding force and consequently the velocity decreases as the estimations of M rise. Also, more heat is generated during this process, and hence temperature grows. Upon enhancing rotation parameter ω, the velocity and temperature profiles are observed to increase along χ in Figs. 12, 13, 14 for momo, hybrid and tri-HNFs. Figure 12 displays that through higher estimations of the parameter ω, the radial velocity tends to rise, and the viscosity of the energy boundary layer declines. It demonstrates that centrifugal force causes the nanofluid particles to be pushed in the radial direction. As a consequence, the velocity in this direction enhances. The profiles of azimuthal speed and heat inside the boundary layer escalate with the escalating estimations of the parameter ω, as seen in Figs. 13 and 14. Additionally, it is observed that when the disk's rotation speed enhances, the thickness of the thermal boundary layer decays. The inspiration of Hall's current parameter ma at the velocity and temperature distributions is revealed in Figs. 15, 16, 17. It is checked that the distributions are escalating with growing estimations of the parameter ma. This suggests that the radial and azimuthal flows are accelerated throughout the boundary layer domain. Also, the enhancement in temperature in Fig. 17 for tri-HNF is slightly further than the memo and HNFs. The effects of the solid volume fraction of memo ϕ_1, hybrid ϕ_2 and tri-hybrid ϕ_3 nanofluids on the velocity and temperature profiles are described in Figs. 18, 19, 20. The radial, azimuthal and temperature profiles are observed to enhance upon the enhancing values of parameters ϕ_1, ϕ_2 and ϕ_3. Physically, this is understood to mean that as the quantity of nanoparticles rises, so does the thermal conductivity as determined by Brinkman with the thermal conductivity model called the Maxwell model. As a consequence, the thermal boundary layer escalates. The escalation in the Prandtl number Pr in Fig. 21 leads to a decrement in the temperature profile. The thickness of the boundary layer reduces as the parameter Pr grows. The Prandtl number is generally the proportion of the heat diffusivity to momentum diffusivity. In heat transmission problems, Pr regulates the relative thickness of momentum and thermal boundary layers. Upon higher estimations
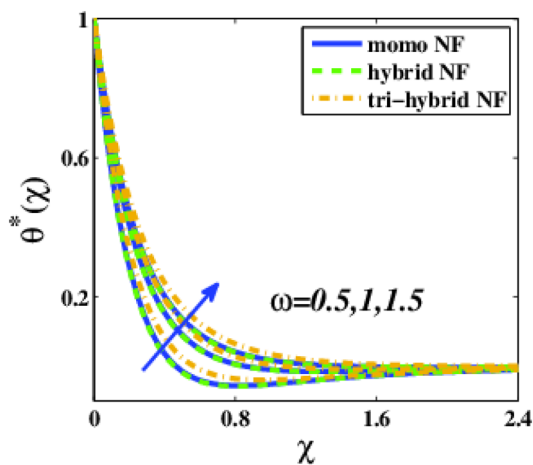
**Figure 14.** Stimulus of ω on $\theta^*(\chi)$.
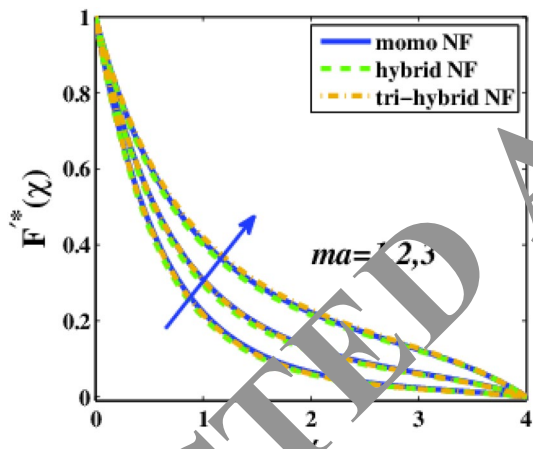

Figure 15. Impression of ma on $F^{*\prime}(\chi)$.
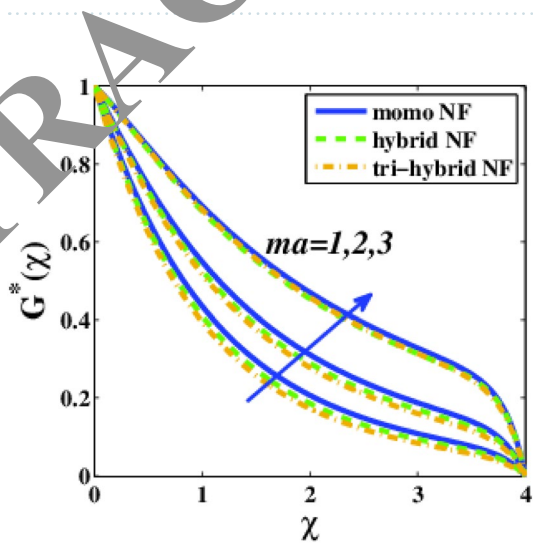
Figure 16. Effect of ma on $G^*(\chi)$.
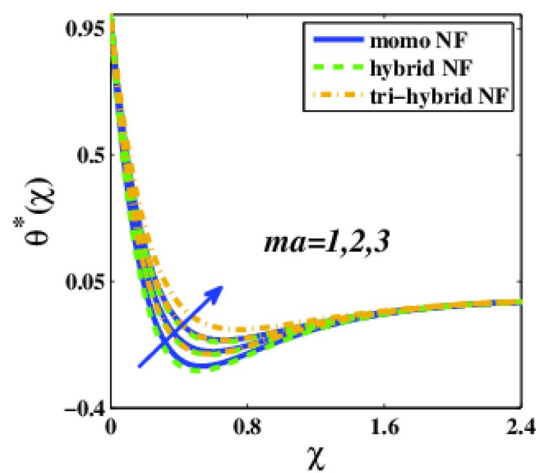
Figure 17. Control of ma on $\theta^*(\chi)$.
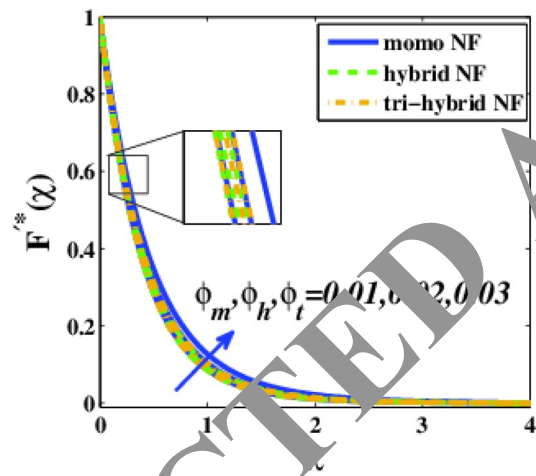
Figure 18. Impact of ϕ on $F^{*'}(\chi)$.
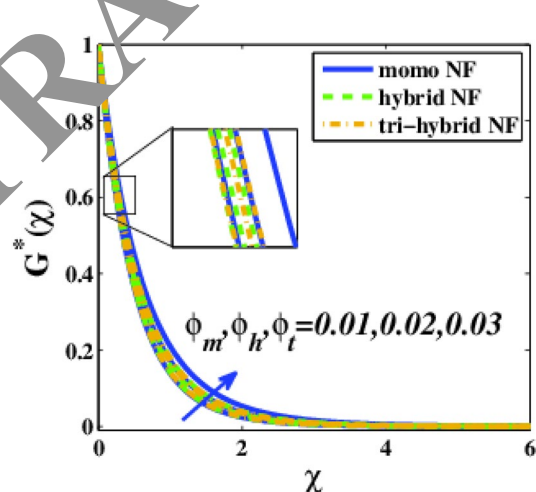
**Figure 19.** Encouragement of ϕ on $G^*(\chi)$.
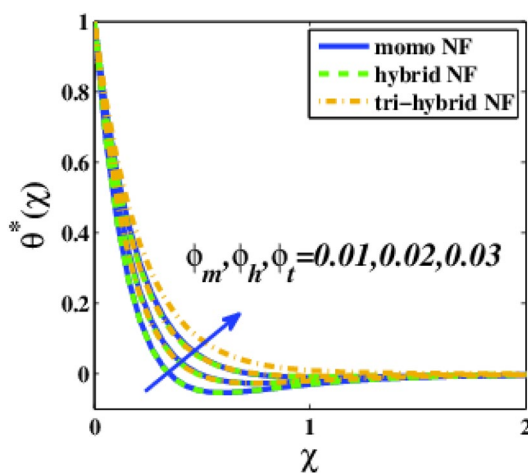
Figure 20. Power of ϕ on $\theta^*(\chi)$.
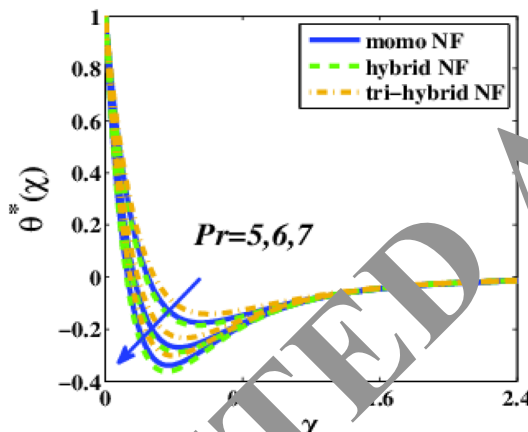

Figure 21. Control of Pr on $\theta^*(\chi)$.
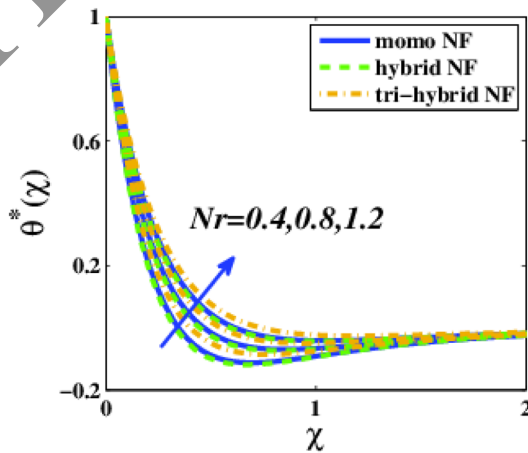

**Figure 22.** Result of Nr on $\theta^*(\chi)$.
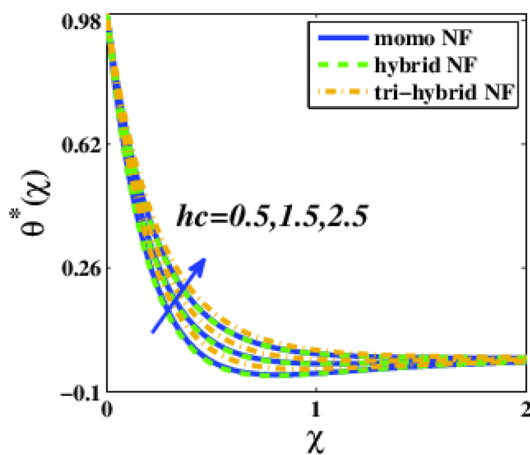
**Figure 23.** Bearing of hc on $\theta^*(\chi)$.
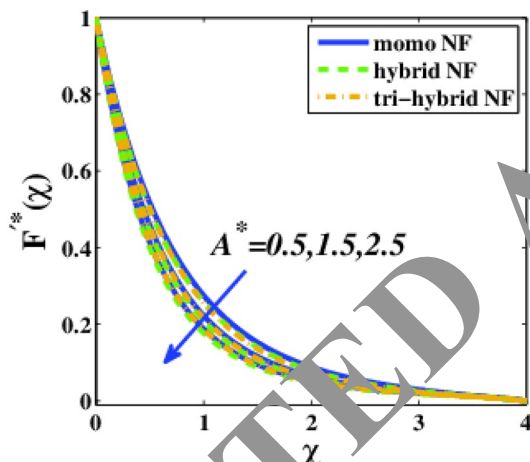
Figure 24. Impact of A^* on $F^*(\chi)$.

of the radiation parameter Nr, the temperature escalates in Fig. 22. The increment in the radiation parameter means the reduction in the mean preoccupation coefficient, which provides extra heat towards fluid and, as a consequence, fluid temperature grows. The rise in the Eckert number hc causes an increment in temperature in Fig. 23. This occurs because frictional heating causes heat to be created within the fluid as hc rises. Eckert number in terms of physics is the ratio of kinetic energy to the particular enthalpy difference between fluid and wall. As a result, a rise in the parameter hc results in work being done against the viscous fluid stresses, which converts kinetic energy into internal energy. An augmentation in the parameter hc implies a conversion of the kinetic energy into internal energy through the effort against the viscous fluid stresses. As a consequence, rising hc rises the fluid's temperature. The impression of the measure of unsteadiness parameter A^* proceeding the velocity and temperature curves are described in Figs. 24, 25, 26 along χ. In Figs. 24 and 25, it is shown that as the parameter A^* grows, the velocity profiles decelerate, whereas temperature accelerates. In the case of radial velocity in Fig. 24, the decrease for a hybrid is slightly higher, whereas, for azimuthal velocity in Fig. 25, the decrease for tri-hybrid is more.

Table discussion. The numerical values of the radial and azimuthal direction skin friction coefficients (surface drag forces) are calculated for NF, HNF and tri-HNF. The values are calculated for diverse ranges of the parameters ϕ, A^*, ma, Ha and ω. Also, the local Nusselt number (heat transfer amount) is numerically calculated in Tables 3 and 4 for the parameters ϕ, hc, Nr, Ha and ma, and the results are compared for nanofluid, hybrid nanofluid and tri-hybrid nanofluid.

Final outcomes

The current theoretical analysis is keen to analyze the stagnant time-dependent flow of simple nanofluid, HNF and THNFs movement over a rotatory stretchable disk. Heat transmission is likewise examined in MHD, thermal radiation, heat dissipation and Hall current. The boundary layer approximation is utilized to design the liquid
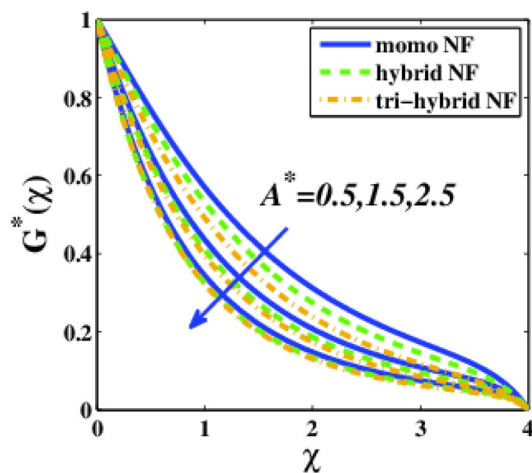
Figure 25. Impression of A^* on $G^*(\chi)$.
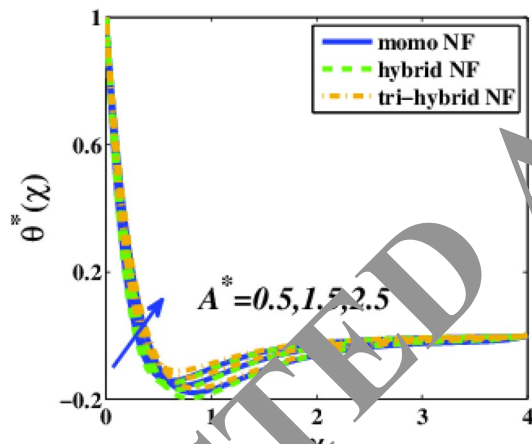
Figure 26. Effect of A^* on $\theta^*(\chi)$.

		Nanofluid	Hybrid nanoparticles	Tri-hybrid nanoparticles
		$-(R_e)^{-\frac{1}{2}} Nu_r$	$-(R_e)^{-\frac{1}{2}} Nu_r$	$-(R_e)^{-\frac{1}{2}} Nu_r$
ϕ	0.01	7.58966	7.61486	7.61865
	0.02	7.79826	7.93460	7.99322
	0.03	7.98996	8.33509	8.43376
hc	0.5	7.79826	8.06540	8.43376
	1.5	10.46771	10.86594	11.21947
	2.5	13.13716	13.66648	14.00518
Nr	0.4	8.59231	8.91928	9.39683
	0.8	9.95131	10.37824	11.04403
	1.2	11.10368	11.61257	12.43686
Ha	0.5	7.14892	7.38443	7.80448
	1	7.24889	7.48980	7.90178
	1.5	7.39344	7.64173	8.04212
ma	1	7.79826	8.06540	8.43376
	2	7.41719	7.66740	8.06633
	3	7.12819	7.36370	7.78644

Table 4. Comparison imitations among NF, HNFs and tri-HNFs of Nusselt number.

movement dynamics in PDEs. The governing PDEs are transfigured into ODEs through precise resemblance variables. The resultant ODEs are mathematically confronted via the efficient Keller Box method. The following outcomes may be depicted from the present investigation:

- The entropy production is increased for the parameters Ha and Nr, but it is decreased for ma and Br.
- The radial and azimuthal velocities are in the similar increasing pattern for the parameters ω, ma and ϕ, whereas decreasing for Ha and A^*.
- The temperature is escalated for the parameters $Ha, \omega, ma, \phi, Nr, hc, A^*$ and decayed for Pr.
- As a result of an incremental change in the volume fraction of nanoparticles, the heat delivery rate of fluid increases in the case of trihybrid nanomolecules compared to dihybrid nanomolecules.
- It has been discovered that the Nusselt number of ternary hybrid nanofluid is increasing when compared to unitary NF and HNF.
- The skin frictions rise by increasing nanoparticles volume fraction values and decrease with increasing values of Hall current parameter.

Future direction.   The current theoretical investigation is presented over a disk geometry. The same investigation can be done over different surfaces like a cylinder, cone and Riga. In the future, a range of physical and technical difficulties might be addressed using the KBM technique[96–107].

Date availability
All data generated or analyzed during this study are included in this published article.

References
1. Cai, S., Wang, Z., Wang, S., Perdikaris, P. & EmKarniadakis, G. Physics informed neural networks for heat transfer problems. *J. Heat Transfer* **143**, 6 (2021).
2. Mousa, M. H., Miljkovic, N. & Nawaz, K. Review of heat transfer enhancement techniques for single phase flows. *Renew. Sustain. Energy Rev.* **137**, 110566 (2021).
3. Li, Y. *et al.* Transforming heat transfer with thermal metamaterials and devices. *Nat. Rev. Mater.* **6**(6), 488–507 (2021).
4. Khodadadi, M. & Sheikholeslami, M. Heat transfer efficiency and electrical performance evaluation of photovoltaic unit under influence of NEPCM. *Int. J. Heat Mass Transfer* 122232 (2022).
5. Sheikholeslami, M. *et al.* Modification for helical turbulator to augment heat transfer behavior of nanomaterial via numerical approach. *Appl. Thermal Eng.* **182**, 115935 (2021).
6. Nguyen, D. H. & SeonAhn, H. A comprehensive review on micro/nanoscale surface modification techniques for heat transfer enhancement in heat exchanger. *Int. J. Heat Mass Transfer* **178**, 121601 (2021).
7. Mohankumar, D., Pazhaniappan, Y., Nitesh Kumar, R.A., Ragul, R., Manoj Kumar, P., & Nikhil Babu, P. Computational study of heat-transfer in extended surfaces with various geometries. In *IOP Conference Series: Materials Science and Engineering*, vol. 1059, no. 1, p. 012055. IOP Publishing (2021).
8. Zhang, X. & Zhang, Y. Experimental study on enhanced heat transfer and flow performance of magnetic nanofluids under alternating magnetic field. *Int. J. Therm. Sci.* **164**, 106897 (2021).
9. Lipiński, W. *et al.* Progress in heat transfer research for high-temperature solar thermal applications. *Appl. Thermal Eng.* **184**, 116137 (2021).
10. Yang, S., Wang, J., Dai, G., Yang, F. & Huang, J. Controlling macroscopic heat transfer with thermal metamaterials: Theory, experiment and application. *Phys. Rep.* **908**, 1–65 (2021).
11. Jiaqiang, E. *et al.* A comprehensive review on performance improvement of micro energy mechanical system: Heat transfer, micro combustion and energy conversion. *Energy* **239**, 122509 (2022).
12. Gao, J., Hu, Z., Yang, Q., Liang, X. & Wu, H. Fluid flow and heat transfer in microchannel heat sinks: Modelling review and recent progress. *Therm. Sci. Eng. Progress* 10, 1203 (2022).
13. Ajarostaghi, M. *et al.* A review of recent passive heat transfer enhancement methods. *Energies* **15**(3), 986 (2022).
14. Said, Z. *et al.* Recent advances on the fundamental physical phenomena behind stability, dynamic motion, thermophysical properties, heat transport, applications, and challenges of nanofluids. *Phys. Rep.* **1**, 1 (2021).
15. Mandal, D. K. *et al.* "Thermo-fluidic transport process in a novel M-shaped cavity packed with non-Darcian porous medium and hybrid nanofluid: Application of artificial neural network (ANN). *Phys. Fluids* **34**(3), 033608 (2022).
16. Saha, A., Manna, N. K., Ghosh, K. & Biswas, N. "Analysis of geometrical shape impact on thermal management of practical fluids using square and circular cavities. *Eur. Phys. J. Spec. Top.* **1**, 1–29 (2022).
17. Al-Chlaihawi, K. K., Alaydamee, H. H., Faisal, A. E., Al-Farhany, K. & Alomari, M. A. Newtonian and non-Newtonian nanofluids with entropy generation in conjugate natural convection of hybrid nanofluid-porous enclosures: A review. *Heat Transfer* **51**(2), 1725–1745 (2022).
18. Kursus, M., Liew, P. J., CheSidik, N. A. & Wang, J. Recent progress on the application of nanofluids and hybrid nanofluids in machining: A comprehensive review. *Int. J. Adv. Manuf. Technol.* **1**, 1–27 (2022).
19. Xiong, Q. *et al.* A comprehensive review on the application of hybrid nanofluids in solar energy collectors. *Sustain. Energy Technol. Assess.* **47**, 101341 (2021).
20. Muneeshwaran, M., Srinivasan, G., Muthukumar, P. & Wang, C. C. Role of hybrid-nanofluid in heat transfer enhancement—A review. *Int. Commun. Heat Mass Transfer* **125**, 105341 (2021).
21. Dubey, V. & Sharma, A. K. A short review on hybrid nanofluids in machining processes. *Adv. Mater. Process. Technol.* **1**, 1–14 (2022).
22. Hussain, S. M. & Jamshed, W. A comparative entropy based analysis of tangent hyperbolic hybrid nanofluid flow: Implementing finite difference method. *Int. Commun. Heat Mass Transfer* **129**, 105671 (2021).
23. Qureshi, M. A. Thermal capability and entropy optimization for Prandtl-Eyring hybrid nanofluid flow in solar aircraft implementation. *Alex. Eng. J.* **61**(7), 5295–5307 (2022).
24. Jamshed, W. *et al.* A brief comparative examination of tangent hyperbolic hybrid nanofluid through a extending surface: Numerical Keller-Box scheme. *Sci. Rep.* **11**(1), 1–32 (2021).

25. Parvin, S. *et al.* Numerical treatment of 2D-Magneto double-diffusive convection flow of a Maxwell nanofluid: Heat transport case study. *Case Stud. Therm. Eng.* **28**, 101383 (2021).
26. Sahu, M., Sarkar, J. & Chandra, L. Steady-state and transient hydrothermal analyses of single-phase natural circulation loop using water-based tri-hybrid nanofluids. *AIChE J.* **67**(6), e17179 (2021).
27. Safiei, W., Rahman, M. M., Yusoff, A. R., Arifin, M. N. & Tasnim, W. Effects of SiO2-Al2O3-ZrO2 tri-hybrid nanofluids on surface roughness and cutting temperature in end milling process of aluminum alloy 6061–T6 using uncoated and coated cutting inserts with minimal quantity lubricant method. *Arab. J. Sci. Eng.* **46**(8), 7699–7718 (2021).
28. Manjunatha, S., Puneeth, V., Gireesha, B. J. & Chamkha, A. Theoretical study of convective heat transfer in ternary nanofluid flowing past a stretching sheet. *J. Appl. Comput. Mech.* **8**(4), 1279–1286 (2022).
29. Gul, T. & Saeed, A. Nonlinear mixed convection couple stress tri-hybrid nanofluids flow in a Darcy-Forchheimer porous medium over a nonlinear stretching surface. *Waves Random Complex Media* **1**, 1–18 (2022).
30. Ramadhan, A. I., Azmi, W.H., Mamat, R., Hamid, K.A., & Norsakinah, S. Investigation on stability of tri-hybrid nanofluids in water-ethylene glycol mixture. In *IOP Conference Series: Materials Science and Engineering*, vol. 469, no. 1, p. 012068. IOP Publishing (2019).
31. Ramadhan, A. I. & HamzahAzmi, W. Experimental investigation of thermo-physical properties of tri-hybrid nanoparticles in water-ethylene glycol mixture. *Walailak J. Sci. Technol.* **18**(8), 9335–9315 (2021).
32. Ramadhan, A. I., HamzahAzmi, W., Mamat, R., Diniardi, E. & Hendrawati, T. Y. Experimental investigation of cooling performance in automotive radiator using Al2O3-TiO2-SiO2 nanofluids. *Autom. Exp.* **5**(1), 28–39 (2022).
33. Zahan, I., Nasrin, R., & Khatun, S. Thermal performance of tri-hybrid nanofluids through a convergent-divergent nozzle using distilled water-ethylene glycol mixtures. Available at SSRN 4097515.
34. Zhu, J. & Holmedal, L. E. A numerical study of separation and stagnation points for steady and unsteady flow over an elliptic cylinder near a moving wall. *Phys. Fluids* **33**(8), 083617 (2021).
35. Carvalho, V. *et al.* Numerical study of the unsteady flow in simplified and realistic iliac bifurcation models. *Fluids* **6**(8), 284 (2021).
36. Ciloglu, D. Numerical simulation of the unsteady flow field in the human pulmonary acinus. *Sādhanā* **46**(4), 1–12 (2021).
37. Javaid, M. *et al.* Unsteady flow of fractional Burgers' fluid in a rotating annulus region with power law kernel. *Alex. Eng. J.* **61**(1), 17–27 (2022).
38. Zhang, F. *et al.* Description of unsteady flow characteristics in a side channel pump with a convex blade. *J. Fluids Eng.* **143**, 4 (2021).
39. Phan, H. M. & He, L. Efficient steady and unsteady flow modeling for arbitrarily mis-staggered bladerow under influence of inlet distortion. *J. Eng. Gas Turbines Power* **143**, 7 (2021).
40. Mariotti, A., Galletti, C., Brunazzi, E. & Salvetti, M. V. Unsteady flow regimes in arrow-shaped micro-mixers with different tilting angles. *Phys. Fluids* **33**(1), 012008 (2021).
41. Gu, P., Han, J., Chen, D. Z. & Wang, C. Reconstructing unsteady flow data from representative streamlines via diffusion and deep-learning-based denoising. *IEEE Comput. Graphics Appl.* **41**(6), 111–121 (2021).
42. Chen, Y., Li, J., Wang, Z., Yan, Y. & Cui, J. Unsteady flow characteristics of an oscillating piezoelectric fan blade at high reynolds numbers. *Appl. Sci.* **11**(20), 9510 (2021).
43. Li, F., Wang, P., He, C. & Liu, Y. Dynamic delayed detached-eddy simulation and acoustic analogy analysis of unsteady flow through a sudden expansion pipe. *J. Vis.* 1–17 (2022).
44. Suliman, M., Ibrahim, M. & Saeed, T. Improvement of efficiency and PEC of parabolic solar collector containing EG-Cu-SWCNT hybrid nanofluid using internal helical fins. *Sustain. Energy Technol. Assess.* **52**, 102111 (2022).
45. Hafeez, M. B., Krawczuk, M., Sabir, S., Jamshed, W. & Pasha, A. A. A finite element analysis of thermal energy inclination based on ternary hybrid nanoparticles influenced by induced magnetic field. *Int. Commun. Heat Mass Transfer* **135**, 106074 (2022).
46. Haneef, M., Madkhali, H. A., Salmi, A., Alharbi, S. O. & Malik, M. Y. Numerical study on heat and mass transfer in Maxwell fluid with tri and hybrid nanoparticles. *Int. Commun. Heat Mass Transfer* **135**, 106061 (2022).
47. Nazir, U., Saleem, A., Al-Zubaidi, A., Shahzadi, I. & Feroz, N. Thermal and mass species transportation in tri-hybridized Sisko martial with heat source over vertical heated cylinder. *Int. Commun. Heat Mass Transfer* **134**, 106003 (2022).
48. Nazir, U. *et al.* A dynamic assessment of various non-Newtonian models for ternary hybrid nanomaterial involving partially ionized mechanism. *Sci. Rep.* **12**(1), 1–15 (2022).
49. Alharbi, K. A. *et al.* Computational valuation of darcy ternary-hybrid nanofluid flow across an extending cylinder with induction effects. *Micromachines* **13**(4), 588 (2022).
50. Xu, H. J., Xing, Z. B., Wang, F. Q. & Cheng, Z. M. Review on heat conduction, heat convection, thermal radiation and phase change heat transfer of nanofluids in porous media: Fundamentals and applications. *Chem.Eng. Sci.* **195**, 462–483 (2019).
51. Wakif, A., Chamkha, A. & Thirupathi Thumma, I. L. Thermal radiation and surface roughness effects on the thermo-magneto-hydrodynamic stability of alumina–copper oxide hybrid nanofluids utilizing the generalized Buongiorno's nanofluid model. *J. Thermal Anal. Calorimetry* **143**(2), 1201–1220 (2021).
52. Chen, J., Zhao, C. Y. & Wang, B. X. Effect of nanoparticle aggregation on the thermal radiation properties of nanofluids: An experimental and theoretical study. *Int. J. Heat Mass Transf.* **154**, 119690 (2020).
53. Agrawal, P. *et al.* Magneto Marangoni flow of γ-AL2O3 nanofluids with thermal radiation and heat source/sink effects over a stretching surface embedded in porous medium. *Case Stud. Thermal Eng.* **23**, 100802 (2021).
54. Prakash, J., Siva, E. P., Tripathi, D., Kuharat, S. & Anwar Bég, O. Peristaltic pumping of magnetic nanofluids with thermal radiation and temperature-dependent viscosity effects: Modelling a solar magneto-biomimetic nanopump. *Renew. Energy* **133**, 1308–1326 (2019).
55. Khan, S. A. *et al.* Magnetic dipole and thermal radiation impacts on stagnation point flow of micropolar based nanofluids over a vertically stretching sheet: Finite element approach. *Processes* **9**(7), 1089 (2021).
56. Ali, L. *et al.* A comparative study of unsteady MHD Falkner-Skan wedge flow for non-Newtonian nanofluids considering thermal radiation and activation energy. *Chin. J. Phys.* **77**, 1625–1638 (2022).
57. Shaw, S., Samantaray, S. S., Misra, A., Nayak, M. K. & Makinde, O. D. Hydromagnetic flow and thermal interpretations of Cross hybrid nanofluid influenced by linear, nonlinear and quadratic thermal radiations for any Prandtl number. *Int. Commun. Heat Mass Transfer* **130**, 105816 (2022).
58. Ramzan, M. *et al.* Analysis of the partially ionized kerosene oil-based ternary nanofluid flow over a convectively heated rotating surface. *Open Phys.* **20**(1), 507–525 (2022).
59. Wang, F. *et al.* A Galerkin strategy for tri-hybridized mixture in ethylene glycol comprising variable diffusion and thermal conductivity using non-Fourier's theory. *Nanotechnol. Rev.* **11**(1), 834–845 (2022).
60. Sohail, M. *et al.* A study of triple-mass diffusion species and energy transfer in Carreau-Yasuda material influenced by activation energy and heat source. *Sci. Rep.* **12**(1), 1–17 (2022).
61. Sohail, M. *et al.* Finite element analysis for ternary hybrid nanoparticles on thermal enhancement in pseudo-plastic liquid through porous stretching sheet. *Sci. Rep.* **12**(1), 1–13 (2022).
62. Nazir, U., Sohail, M., Hafeez, M. B. & Krawczuk, M. Significant production of thermal energy in partially ionized hyperbolic tangent material based on ternary hybrid nanomaterials. *Energies* **14**(21), 6911 (2021).

63. Khan, M. N., Ahmad, S. & Nadeem, S. Flow and heat transfer investigation of bio-convective hybrid nanofluid with triple stratification effects. *Phys. Script.* **96**(6), 5210 (2021).
64. Zainal, N. A., Nazar, R., Naganthran, K. & Pop, I. Viscous dissipation and MHD hybrid nanofluid flow towards an exponentially stretching/shrinking surface. *Neural Comput. Appl.* **33**(17), 11285–11295 (2021).
65. Hou, E. *et al.* Dynamics of tri-hybrid nanoparticles in the rheology of pseudo-plastic liquid with dufour and soret effects. *Micromachines* **13**(2), 201 (2022).
66. Khan, U., Adnan, A. & Haleema, B. Thermal performance in nanofluid and hybrid nanofluid under the influence of mixed convection and viscous dissipation: numerical investigation. *Waves Random Complex Media* **1**, 1–19 (2022).
67. Munawar, S. & Saleem, N. Mixed convective cilia triggered stream of magneto ternary nanofluid through elastic electroosmotic pump: A comparative entropic analysis. *J. Mol. Liquids* **352**, 118662 (2022).
68. Feroz, N., Shah, Z., Islam, S., Alzahrani, E. O. & Khan, W. Entropy generation of carbon nanotubes flow in a rotating channel with hall and ion-slip effect using effective thermal conductivity model. *Entropy* **21**, 52 (2019).
69. Shahsavar, A., Sardari, P. T. & Toghraie, D. Free convection heat transfer and entropy generation analysis of water-Fe3O4/CNT hybrid nanofuid in a concentric annulus. *Int. J. Numer Methods Heat Fluid Flow* **29**(3), 915–934 (2019).
70. Hussien, A. A. *et al.* Heat transfer and entropy generation abilities of MWCNTs/GNPs hybrid nanofuids in microtubes. *Entropy* **21**(5), 480 (2019).
71. Ellahi, R., Alamri, S. Z., Basit, A. & Majeed, A. Effects of MHD and slip on heat transfer boundary layer fow over a moving plate based on specific entropy generation. *J. Taibah Univ. Sci.* **12**(4), 476–482 (2018).
72. Lu, D., Ramzan, M., Ahmad, S., Shafee, A. & Suleman, M. Impact of nonlinear thermal radiation and entropy optimization coatings with hybrid nanoliquidflow past a curved stretched surface. *Coatings* **8**(12), 430 (2018).
73. Khan, N. S., Zuhra, S. & Shah, Q. Entropy generation in two phase model for simulating flow and heat transfer of carbon nanotubes between rotating stretchable disks with cubic autocatalysis chemical reaction. *Appl. Nanosci.* **9**(8), 1797–1822 (2019).
74. Sheikholeslami, M., Ellahi, R., Shafee, A. & Li, Z. Numerical investigation for second law analysis of ferrofuid inside a porous semi annulus. *Int. J. Numer Methods Heat Fluid Flow* **29**(3), 1079–1102 (2019).
75. Zeeshan, A., Shehzad, N., Abbas, T. & Ellahi, R. Efects of radiative electro-magnetohydrodynamics diminishing internal energy of pressure-driven fow of titanium dioxide-water nanofuid due to entropy generation. *Entropy* **21**(3), 236 (2019).
76. Ahmad, S., Nadeem, S. & Ullah, N. Entropy generation and temperature dependent viscosity in the study of SWCNT–MWCNT hybrid nanofluid. *Appl. Nanosci.* **10**(12), 5107–5119 (2020).
77. Moghadasi, H., Malekian, N., Aminian, E. & Saffari, H. Thermodynamic analysis of entropy generation due to energy transfer through circular surfaces under pool boiling condition. *J. Therm. Anal. Calorimetry* **1**, 1–14 (2021).
78. Jamshed, W., Nisar, K. S., Ibrahim, R. W., Shahzad, F. & Eid, M. R. Thermal expansion optimization in solar aircraft using tangent hyperbolic hybrid nanofluid: A solar thermal application. *J. Mater. Res. Technol.* **14**, 985–1006 (2021).
79. Jamshed, W. *et al.* Computational frame work of Cattaneo–Christov heat flux effects on Engine Oil based Williamson hybrid nanofluids: A thermal case study. *Case Stud. Therm. Eng.* **26**, 1179 (2021).
80. Shahzad, F. *et al.* Raising thermal efficiency of solar water-pump using Oldroyd-B nanofluids' flow: An optimal thermal application. *Energy Sci. Eng.* **1**, 1 (2022).
81. Acharya, N. On the hydrothermal behavior and entropy analysis of buoyancy driven magnetohydrodynamic hybrid nanofluid flow within an octagonal enclosure fitted with fins: application to thermal energy storage. *J. Energy Stor.* **53**, 105198 (2022).
82. Acharya, N., Mabood, F. & Badruddin, I. A. Thermal performance of unsteady mixed convective Ag/MgO nanohybrid flow near the stagnation point domain of a spinning sphere. *Int. Commun. Heat Mass Transfer* **134**, 106019 (2022).
83. Acharya, N. Buoyancy driven magnetohydrodynamic hybrid nanofluid flow within a circular enclosure fitted with fins. *Int. Commun. Heat Mass Transfer* **133**, 105980 (2022).
84. Acharya, N., Maity, S., & Kundu, P. K. Entropy generation optimization of unsteady radiative hybrid nanofluid flow over a slippery spinning disk. *Proc. Inst. Mech. Eng. Part C J. Mech. Eng. Sci.* 09544062211065384 (2022).
85. Acharya, N. On the flow patterns and thermal control of radiative natural convective hybrid nanofluid flow inside a square enclosure having various shaped multiple heated obstacles. *Eur. Phys. J. Plus* **136**(8), 1–29 (2021).
86. Acharya, N. & Mabood, F. On the hydrothermal features of radiative Fe3O4–graphene hybrid nanofluid flow over a slippery bended surface with heat source/sink. *J. Therm. Anal. Calorim.* **143**(2), 1273–1289 (2021).
87. Acharya, N. On the flow patterns and thermal behaviour of hybrid nanofluid flow inside a microchannel in presence of radiative solar energy. *J. Therm. Anal. Calorim.* **141**(4), 1425–1442 (2020).
88. Kumar, A., & Ray, R.K. Shape effect of nanoparticles and entropy generation analysis for magnetohydrodynamic flow of (Al₂O₃-H₂O) hybrid nanomaterial under the influence of hall current. *Indian J. Phys.* (2022).
89. Puneeth, V. *et al.* Implementation of modified Buongiorno's model for the investigation of chemically reacting rGO-Fe₃O₄-TiO₂-H₂O ternary nanofluid jet flow in the presence of bio-active mixers. *Chem. Phys.Lett.* **786**, 139194 (2022).
90. Hayat, T., Nadeem, S. & Khan, A. U. Rotating flow of Ag-CuO/H2O hybrid nanofluid with radiation and partial slip boundary effects. *Eur.Phys. J. E* **41**(6), 1–9 (2018).
91. Adnan, A. & Ashraf, W. Thermal efficiency in hybrid (Al2O3-CuO/H2O) and ternary hybrid nanofluids (Al2O3-CuO-Cu/H2O) by considering the novel effects of imposed magnetic field and convective heat condition. *Waves Random Complex Media* **1**, 1–16 (2022).
92. Arikoglu, A., Ozkol, I. & Komurgoz, G. Effect of slip on entropy generation in a single rotating disk in MHD flow. *Appl. Energy* **85**(12), 1225–1236 (2008).
93. Keller, H.B. 'A new difference scheme for parabolic problems. in *Numerical Solution of Partial Differential Equations–II* (Elsevier) (1971).
94. Jamshed, W., Nasir, N. A. A. M., Brahmia, A., Nisar, K. S. & Eid, M. R. Entropy analysis of radiative [MgZn6Zr-Cu/EO] Casson hybrid nanoliquid with variant thermal conductivity along a stretching surface: Implementing Keller box method. *Proc. Int. Mech. Eng. Part C J. Mech. Eng. Sci.* **954**, 4062 (2022).
95. Bachok, N., Ishak, A. & Pop, I. Flow and heat transfer over a rotating porous disk in a nanofluid. *Phys. B* **406**, 1767–1772 (2011).
96. Turkyilmazoglu, M. Nanofluid flow and heat transfer due to a rotating disk. *Comput. Fluids* **94**, 139–146 (2014).
97. Raizah, Z., Khan, A., Awan, A. S. S. H., Galal, A. M. & Weera, W. Time-dependent fractional second-grade fluid flow through a channel influenced by unsteady motion of a bottom plate. *J. AIMS Math.* **8**, 1 (2023).
98. Algehyne, E. A., Aldhabani, M. S., Saeed, A., Dawar, A. & Kumam, P. Mixed convective flow of Casson and Oldroyd-B fluids through a stratified stretching sheet with nonlinear thermal radiation and chemical reaction. *J. Taibah Univ. Sci.* **16**(1), 193–203 (2022).
99. Shamshuddin, M. D., Akkurt, N., Saeed, A. & Kumam, P. Radiation mechanism on dissipative ternary hybrid nanoliquid flow through rotating disk encountered by Hall currents: HAM solution. *Alex. Eng. J.* **1**, 1 (2022).
100. Algehyne, E. A. *et al.* Framing the hydrothermal significance of water-based hybrid nanofluid flow over a revolving disk. *Int. J. Nonlinear Sci. Numer. Simul.* **1**, 1 (2022).
101. Pasha, A. A. *et al.* Statistical analysis of viscous hybridized nanofluid flowing via Galerkin finite element technique. *Int. Commun. Heat Mass Transfer* **137**, 106244 (2022).

102. Hussain, S. M., Jamshed, W., Pasha, A. A., Adil, M. & Akram, M. Galerkin finite element solution for electromagnetic radiative impact on viscid Williamson two-phase nanofluid flow via extendable surface. *Int. Commun. Heat Mass Transfer* **137**, 106243 (2022).
103. Hafeez, M. B., Krawczuk, M., Nisar, K. S., Jamshed, W. & Pasha, A. A. A finite element analysis of thermal energy inclination based on ternary hybrid nanoparticles influenced by induced magnetic field. *Int. Commun. Heat Mass Transfer* **135**, 106074 (2022).
104. Jamshed, W. *et al.* Physical specifications of MHD mixed convective of Ostwald-de Waele nanofluids in a vented-cavity with inner elliptic cylinder. *Int. Commun. Heat Mass Transfer* **134**, 106038 (2022).
105. Shah, N. A., Wakif, A., El-Zahar, E. R., Ahmad, S. & Yook, S. J. Numerical simulation of a thermally enhanced EMHD flow of a heterogeneous micropolar mixture comprising (60%)-ethylene glycol (EG), (40%)-water (W), and copper oxide nanomaterials (CuO). *Case Stud. Thermal Eng.* **35**, 102046 (2022).
106. Shah, N. A., Wakif, A., El-Zahar, E. R., Thumma, T. & Yook, S. J. Heat transfers thermodynamic activity of a second-grade ternary nanofluid flow over a vertical plate with Atangana-Baleanu time-fractional integral. *Alex. Eng. J.* **61**(12), 10045–10053 (2022).
107. Jamshed, W. *et al.* Experimental and TDDFT materials simulation of thermal characteristics and entropy optimized of Williamson Cu-methanol and Al₂O₃-methanol nanofluid flowing through solar collector. *Sci. Rep.* **12**, 18130 (2022).
108. Dinesh Kumar, M., Raju, C. S. K., Sajjan, K., El-Zahar, E. R. & Shah, N. A. Linear and quadratic convection 3D flow with transpiration and hybrid nanoparticles. *Int. Commun. Heat Mass Transfer* **1**, 1 (2022).

Acknowledgements

Author contributions

Conceptualization: F.S. Formal analysis: E.S.M.T.E.D. Investigation: W.J. Methodology: U. Software: F.S. and R.W.I. Re-graphical representation and adding analysis of data: K.F.A.O. Writing—original draft: E.S.M.T.E.D. Writing—review editing: A.M.A. Numerical process breakdown: K.F.A.O. Re-modelling design: A.M.A. Re-validation: K.F.A.O. and W.J. Furthermore, all the authors equally contributed to the writing and proofreading of the paper. All authors reviewed the manuscript.

Competing interests

Additional information